https://doi.org/10.1016/j.mtener.2018.11.006

Two-dimensional materials in perovskite solar cells

Peng You, Guanqi Tang, Feng Yan*

P. You, G. Q. Tang, and Prof. F. Yan*
Department of Applied Physics, The Hong Kong Polytechnic University, Hung Hom, Kowloon, Hong Kong.
E-mail: apafyan@polyu.edu.hk

Abstract

Organic-inorganic hybrid perovskite solar cells (PSCs) have experienced a rapid development in the past few years, reaching a certified efficiency over 23%. The semiconducting perovskite materials have shown great potential for photovoltaic applications because of their outstanding optoelectronic properties. Meanwhile, two-dimensional (2D) materials have attracted increasing attention due to their exceptional chemical, electrical and physical properties. Recently, the synergic effects due to the combination of 2D materials and organic-inorganic hybrid perovskite materials have been revealed by many groups. In this review, recent works on the applications of 2D materials in PSCs are comprehensively presented and discussed. The progress and advantages of 2D materials as electrodes, charge transport layers and additives in PSCs are systemically reviewed. Finally, critical challenges and prospects of this research field are addressed.

Keywords: perovskite solar cell; two-dimensional material; charge transport material; power conversion efficiency;

1. Introduction

The rapid industrial development and population growth all over the world during the past decades have led to an explosion in the global demand for energy. However, the energy supply is still mainly relying on the fossil fuels like oils and coals, which are known to be limited on the earth and are going to dry up in the near future. Therefore, the increasingly severe energy crisis has urged people to find clean and renewable alternatives to fossil fuels. The solar energy, in contrast, is a very clean and sustainable energy source that can offer inexhaustible supply of energy for human society. Thus, the main challenge now is how to harvest the solar energy in a more efficient way. In the existing technologies for solar energy harvesting, photovoltaics (PV), which directly converts solar energy into electric power, is the most promising strategy to deal with the energy crisis we are facing now.

Solar cells based on organic-inorganic hybrid perovskite materials, have attracted enormous attention during the past few years. Since the first report of the material used in solar cells in 2009,[1] the power conversion efficiencies (PCEs) of perovskite solar cells (PSCs) have now reached a certified value over 23%[2], showing an unprecedented fast growth rate. PSCs have attained comparable photovoltaic performance to copper indium gallium diselenide (CIGS) solar cells (22.9%), and is approaching that of monocrystalline silicon solar cells (26.1% for single-junction silicon cells without concentrators).[2] The hybrid perovskites have been considered to be ideal materials for photovoltaic applications, which are likely attributed to their outstanding optoelectronic properties, ease of processing, and low fabrication costs. Recently, there are more and more reports about the combination of the PSCs with another category of star materials, two-dimensional (2D) materials, like graphene, transition metal dichalcogenides (TMDs) and black phosphorus (BP). Due to the exceptional physical and chemical properties of the perovskites and 2D materials, tremendous improvements have been demonstrated by introduction of 2D materials for the fabrication of PSCs. In this article, we will provide comprehensive review of recent research work about the applications

of 2D materials in PSCs, including the utilization of 2D materials for electrodes, hole transporting, electron transporting and incorporation in perovskite layers. Mechanisms about how the 2D materials can contribute to the improved photovoltaic performances or stabilities of PSCs were discussed. In the first chapter, we will give a brief introduction of the organic-inorganic hybrid perovskite materials, PSCs and 2D materials.

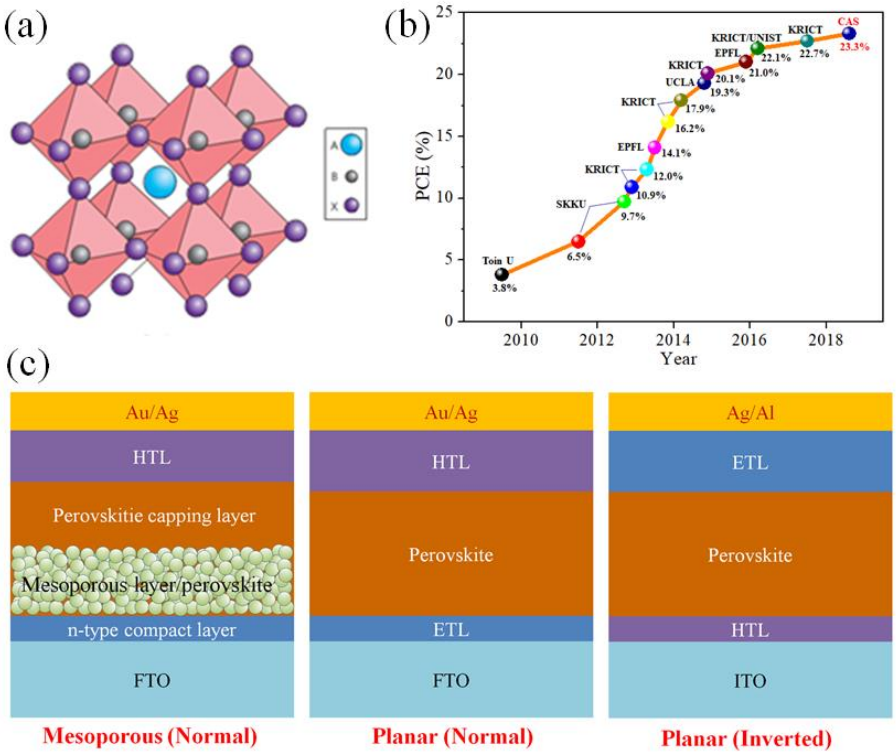

Fig. 1. (a) Schematic diagram of the crystal structure of organic-inorganic hybrid perovskites. Reprinted with permission from ref.[3]. (b) Efficiency roadmap for organic-inorganic hybrid PSCs.[1, 4-13] (c) Schematic illustration of the mesoporous and planar device architectures of PSCs. HTL represents the hole transport layer; and ETL represents the electron transport layer.

1.1 Organic-inorganic hybrid perovskite materials

1.1.1 Properties of organic-inorganic hybrid perovskites

The organic-inorganic hybrid perovskites generally have a chemical formula of ABX_3 (where A is MA or FA, MA= $CH_3NH_3^+$, FA=$CH_3(NH_2)_2^+$; B is Pb^+ or Sn^{2+}; X is Cl^-, Br^- or I^-). In a standard cubic crystal structure, the body-centred cation B has six nearest X anions, while the cation A located at vertex positions possesses twelve nearest

X anions, as shown in Fig. 1a. In order to maintain a stable crystal structure, it is generally accepted that the tolerance factor t (t=(r_A+r_X)/[$2^{1/2}$(r_B+r_X)], where r_A, r_B, r_X represent the effective ionic radii for the ions at A, B and X sites, respectively) should be in the range between 0.813 and 1.107.[14] Thus, for the compositional change of perovskites, the tolerance factor should be carefully considered according to the ion radius of the cations and anions.

Being direct bandgap semiconductors, the hybrid perovskites possess extremely high absorption coefficients, with reported values in the order of 10^5 cm^{-1}.[15] Thus, a perovskite film of ~ 400 nm thick is generally sufficient to absorb sunlight, which greatly reduces the material costs.[16, 17] In contrast to organic photovoltaic materials, the exciton binding energy of organic-inorganic hybrid perovskites was demonstrated to be only 16 meV at low temperatures, and this value falls to even smaller values of only a few millielectronvolts at room temperature, which explains their excellent photovoltaic performance due to spontaneous free-charge separation upon light illumination.[18] The colour of the hybrid halide perovskites is tunable through compositional engineering, covering the entire visible range and part of near infrared region, which can enable the realization of colourful solar cells.[19]

The outstanding performance of PSCs can be partially attributed to the excellent charge transport properties of organometal halide perovskites. The small photocarrier effective masses, high carrier mobilities, long carrier lifetimes, long diffusion lengths and low trap densities ensure that charge carriers can be freely transported across the entire perovskite film (normally several hundred nanometres) before recombination.[20-26] Originally in 2013, the electron and hole diffusion lengths of solution processed $MAPbI_3$ perovskite films were calculated to be around 100 nm (the carrier lifetime is only several nanoseconds) based on the results of transient optical spectroscopy and time-resolved PL-quenching measurements.[23] This value of carrier diffusion length was already much higher than that of the traditional low-temperature solution-

processed light absorbers (typically ~ 10 nm).[23] It was also found that the diffusion lengths of $MAPbI_{3-x}Cl_x$ mixed halide perovskites are larger than 1 μm, which is an order of magnitude greater than the triiodide perovskite absorbers.[22] Owing to the much longer carrier diffusion lengths of mixed halide perovskites than the light absorption depth (100 ~ 200 nm), the mesoporous TiO_2 structure is no longer necessary so that planar structure is adoptable.[22] The charge carrier mobilities of solution-processed organometal trihalide perovskite films are firstly estimated to be around 10 ~ 20 $cm^2V^{-1}s^{-1}$, which is rather high for solution-processed materials.[25, 26] The successful growth of large organometal trihalide perovskite single crystals in 2015 greatly promoted our understanding about the bulk electrical properties of this material.[21, 24, 27] Huang's group reported that the diffusion length in the solution-grown $MAPbI_3$ single crystals can exceed 175 μm under 1 sun illumination, and is larger than 3 μm under weak light condition, which has far exceeded the diffusion length obtained in organometal perovskite thin films.[24] In addition, the carrier mobility they measured in $MAPbI_3$ single crystals was as high as 164 $cm^2V^{-1}s^{-1}$, and the trap density was calculated to be as low as 3.6×10^{10} cm^{-3}.[24] Cooke *et al.* even reported a record high mobility of 800 $cm^2V^{-1}s^{-1}$ on a single crystal lead halide perovskites through optical pump-multi-THz measurements.[27]

The dominating perovskites ($MAPbI_3$) possess a bandgap around 1.5 eV, which is extremely close to the 'ideal' single-junction bandgap (1.1 eV ~ 1.4 eV).[10, 19, 28] Depending on the halide used, the bandgap can be continuously tuned from ~ 1.5 eV (pure I) to ~ 3.2 eV (pure Cl).[10, 19, 29] Even smaller bandgaps can be achieved by using different organic cations or inorganic cations, covering the entire visible spectral range and part of the near infrared region.[16, 29] Bandgap tuning is generally considered to be a good way to extend the absorption to longer wavelengths without sacrificing the absorption coefficient. Replacing MA with other organic cations (e.g., FA, 5-AVA) or inorganic cations (e.g., Cs, Rb) is one approach to realize the bandgap tuning, because changing the organic cations at A sites of AMX_3 perovskites can tune the bandgap by

modifying the metal-halide-metal bond length and angle without affecting the valence band maximum.[30] Partial replacement of MA with FA is an effective way to extend the absorption to longer wavelengths and enhance the thermal stability.[10] With the combination of FA, MA and Cesium (Cs), the resulting triple-cation perovskites are less sensitive to processing conditions, thermally more stable and show higher PCEs with better reproducibility.[13, 31] Besides, the bandgap of the hybrid perovskites can also be continuously tuned from 1.5 eV to 2.3 eV by introducing mixed halides (I and Br).[19] The introduction of bromide element also enhances the stability of the perovskites in ambient conditions. In addition to altering the organic cations and the halide anions, another approach for tuning the bandgap is the direct change or substitution of the metal cations. For instance, the bandgap of $MASn_xPb_{1-x}I_3$ perovskites can be tuned from 1.3 eV to 1.55 eV by varying the molar ratio of lead and tin.[32] Due to concerns about the toxicity of lead, lead-free perovskites such as $MASnX_3$, have attracted increasing attention recently. Compared with the lead-based perovskite, the relatively lower band gap of $MASnI_3$ (~ 1.3 eV) allows light absorption over a much broader range with an increased current density. However, both the efficiency and the stability of the Sn-based devices are still not comparable to that of the lead-based cells at this moment.

1.1.2 Deposition methods of perovskite films

The fabrication of high-quality perovskite films is one the most important processes to achieve high-performance PSCs. So far, a variety of deposition methods have been developed by researchers. The most widely adopted deposition methods for perovskite films can be categorized into three groups: one-step solution process, two-step solution process and vapor-phase deposition.

For standard one-step solution method, the perovskite raw materials including lead sources (PbI_2, $PbCl_2$, etc.) and organic sources (MAI, FAI, etc.) are firstly dissolved in appropriate solvents such as DMF, GBL or DMSO, and the solution was then spin-coated on the substrate. A subsequent thermal annealing process (mostly around 100 ºC)

is needed in most cases for the complete crystallization of the perovskite film. Currently, an anti-solvent assisted one-step solution process has been widely adopted by researchers. During the spin-coating process of the perovskite solution (in mixed solvents of DMF and DMSO), a toluene (or chlorobenzene) dripping process could lead to quite uniform and dense perovskite layers through the formation of intermediate phases (like PbI_2-MAI-DMSO). The role of chlorobenzene is to rapidly reduce the solubility of the perovskites in the mixed solvents and thereby induce fast crystallization, and thus very flat and uniform perovskite films with large grain size could be obtained. To date, this one-step anti-solvent fast crystallization process have already been widely adopted for fabricating perovskite-based solar cells as well as many other optoelectronic devices with high performances.[13, 31, 33-37]

For the two-step solution process in very early stages,[8] PbI_2 solution in DMF is spin-coated on the substrate to form a PbI_2 layer and the film is kept at a low temperature (e.g., 70 ºC) for a certain time. After drying, the film is immersed into a solution of MAI in 2-propanol (e.g., 10 mg/ml) for appropriate time and is then rinsed in pure 2-propanol to wash away the residual MAI. Normally, a further thermal annealing process is also required for crystallization. Gratzel *et al.* firstly adopted this two-step solution process and successfully achieved a certified efficiency of 14.1%.[8] Later, a thermal annealing-induced inter-diffusion method was developed by Huang's group to fabricate pin-hole free perovskite films.[38] The stacked PbI_2/MAI bilayer structure will convert to perovskites upon thermal annealing. A lot of groups later adopted this approach for the fabrication of PSCs with relatively high efficiencies.[12, 39-43]

Thermal evaporation, which is often used to deposit metal electrodes, can also be adopted to fabricate perovskite films. Normally, the lead and organic sources were evaporated simultaneously from two separate ceramic crucibles in an evaporation chamber. The crystallization started immediately after the evaporation. Further thermal annealing was needed to get fully crystallized perovskite films. Compared with solution

processed perovskite films, the vapor-deposited ones were extremely uniform, and the surfaces were quite flat without pin-holes or voids. The solar cell based on the vapor-deposited perovskite film demonstrated an efficiency higher than 15%. The deposition rates of the two precursor materials are crucial for the fabrication of high-quality perovskite films. However, the thermal deposition process requires high vacuum and expensive equipment, which is energy consuming and is incompatible with large-scale mass production. What's more, the growth condition and mechanisms of vapor deposition are relatively complicated, which hinders the large-scale application of this technique.

1.2 Perovskite solar cells

1.2.1 Evolution of PSCs

From the best-research cell efficiencies chart provided by the National Renewable Energy Laboratory (NREL)[2], it is obvious to see that the efficiency of PSCs has been growing at an unprecedented rate, which is faster than that of all the other types of solar cells. Some of the landmark efficiencies during its development process was exhibited in Fig. 1b based on published papers or certified efficiencies. [1, 2, 4-13] In 2009, Miyasaka and co-workers reported the photovoltaic function of the organic-inorganic lead halide perovskite materials for the first time.[1] The perovskite nanocrystalline particles ($MAPbBr_3$ and $MAPbI_3$) self-organized on TiO_2 surface were adopted as visible-light sensitizers in the dye-sensitized solar cells (DSSCs) with liquid electrolyte. A power conversion efficiency of 3.8% on a $MAPbI_3$-based cell was obtained. The efficiency was actually much lower than that of the conventional DSSCs (~ 11%) at that time, and the perovskite compounds showed very poor stability in the liquid electrolytes. Two years later, Park *et al*. fabricated a perovskite quantum-dot-sensitized solar cell with PCE of approximately 6.5% by using 2 ~ 3 nm sized $MAPbI_3$ nanocrystals.[4] However, the lifetime of the perovskite quantum-dot-sensitized solar cell was only about 10 minutes due to the easy dissolution of the perovskite nanocrystals in the liquid electrolyte. Thus, little attention had been paid to the hybrid perovskite materials, until

the successful development of the first all-solid-state mesoscopic solar cells with impressive PCE of 9.7% by Park's group in 2012.[5] The use of a solid hole transport material (spiro-OMeTAD) dramatically improved the efficiency as well as the device stability compared with the former electrolyte-based perovskite sensitized cells. This improvement triggered a quick research explosion on PSCs. Since then, hybrid halide perovskites have attracted enormous attention worldwide. Soon after, in the same year, Snaith and his co-workers pushed the efficiency of PSCs to 10.9% with dramatically improved open circuit voltage (V_{oc}) (0.98 V) by coating a new mixed-halide perovskite ($MAPbI_2Cl$) on the surfaces of a mesostructured insulating Al_2O_3 scaffold, termed as "meso-superstructured solar cell" (MSSC).[6] This iodide-chloride mixed-halide perovskite was found to be more stable in air and possessed better electron diffusion property than the previously reported pure iodide equivalent.

In 2013, Gratzel and Seok *et al*. introduced a layered sandwich-type device structure, comprising of a 3D-nanocomposites of mesoporous TiO_2 scaffold (infiltrated with perovskite material), a dense well-crystallized $MAPbI_3$ perovskite capping layer and a polymeric hole transport layer. By comparison of several different kinds of hole transport materials, they found that polytriarylamine (PTAA) provided the maximum efficiency of 12.0% under standard AM 1.5 light illumination, with a substantially increased fill factor (FF) (72.7%). Later in 2013, Gratzel *et al*. achieved a PCE of 15.0% (the certified efficiency was 14.1%) with improved perovskite morphology through a sequential deposition route (also called two-step method),[8] which was widely adopted by other researchers ever after. This technique for the fabrication of perovskite material increased the reproducibility compared to the previously employed one-step route, and it provided with opportunities for high-performance PSCs. A close PCE of 15.4% with an open-circuit voltage of 1.07 V was illustrated by Snaith and his co-workers by using a sequential vapour-deposited $MAPbI_{3-X}Cl_x$ perovskite layer as the absorbing layer.[44] It was proved that the mesostructured TiO_2 scaffold was not necessary and a simple planar heterojunction thin-film structure can also achieve high photovoltaic performance,

although this device structure tend to show more significant hysteresis phenomenon in current-voltage (*I-V*) characteristics.

Soon afterwards, Seok's research team reported a certified PCE of 16.2% without *I-V* hysteresis by using $MAPb(I_{1-x}Br_x)_3$ as the absorbing layer and PTAA as a hole transport layer.[9] A solvent-engineering technique was developed to obtain extremely dense and uniform perovskite films. Here, a mixed solvent of GBL and DMSO were used to prepare the perovskite precursor solution. The better morphology was attributed to the formation of the intermediate phase PbI_2-MAI(Br)-DMSO film when non-dissolving solvent (such as toluene) was drop-casted during the spin-coating process. For this kind of bilayer architecture, the thickness ratio of the continuous perovskite upper layer and the mp-TiO_2 layer (also infiltrated with perovskites) is the key factor for the brilliant performance. This was further increased to a confirmed PCE of 17.9% also by Soek's group in early 2014.[10] A mixed composition of $(FAPbI_3)_{1-x}(MAPbBr_3)_x$ was used as light absorber. According to their report, the incorporation of $MAPbBr_3$ into $FAPbI_3$ could stabilize the perovskite phase and improved the efficiency. Besides, Yang *et al*. also reported a high efficiency of 19.3% in a planar device geometry by means of a delicate interface engineering throughout the entire device.[11]

In late 2014, Seok and his colleagues reported an exciting PCE of 20.1%,[12] which was the first one that surpassed the 20% mark. The perovskite film was fabricated essentially through a two-step solution process. Unlike the conventional two-step method, the PbI_2 film was replaced by a PbI_2(DMSO) complex film, which will interact with FAI (MABr) in 2-propanol through an intramolecular exchange process (IEP). Negligible volume expansion occurred during the IEP process and high-quality perovskite film was obtained. High efficiency PSCs with average efficiency of over 19% can be obtained through this technique.

In late 2015, Saliba *et al*. reported a higher efficiency of 21.1% by employing a triple-

cation perovskite composition (FA/MA/Cs),[13] which were thermally more stable, and more robust to the fabrication conditions. This provide a novel strategy for the further improvement of PSCs. It was reported that the introduction of additional iodide ions into the perovskite precursor solution can effectively decrease the concentration of deep-level defects in the perovskite layer, yielding a certified PCE of 22.1%. In 2018, a new record efficiency of 23.3% was developed by Chinese Academy of Sciences.[2] Further improvement of the efficiency of PSCs is on the way.

1.2.2 Device architectures of PSCs

The original perovskite solar cells employed a mesoporous structure with a thick mesoporous metal-oxide layer (mp-TiO_2 or mp-Al_2O_3) as scaffold,[1, 4-6, 8] which was evolved from the typical DSSCs. In this structure, the mesoporous scaffold is filled with perovskites and sandwiched between a compact electron transport layer (mostly TiO_2) and a hole transport layer. The mesoporous structure is thought to enhance the charge collection efficiency by decreasing the carrier transport distance. In the very early stage, the thickness of the mesoporous layer was usually larger than 500 nm (or even several micro meters), to absorb sufficient light.[1, 4-6, 8] But because the crystal growth of perovskites is confined by the dimensions of the pores, a great amount of the material is present in disordered or amorphous phases,[45] which will definitely deteriorate the device performance. Interestingly, when the mesoporous layer thickness decreases to less than 300 nm, a dense and uniform perovskite capping layer with large grains will form on top of the porous layer[9, 10, 12, 13], as shown in Fig. 1c. The complete pore filling together with the superior crystallinity of the continuous perovskite capping layer can assure the high charge collection and transport efficiencies. As a result, PSCs based on the mesoporous structure have demonstrated high efficiencies.[9, 10, 12, 13]

Further development of the device architectures brings out the n-i-p or p-i-n planar configurations, which are similar with that of organic solar cells (OPVs). In planar structures, the mesoporous layer is omitted, and the perovskite layer is sandwiched between two opposite charge transport layers (hole transport layer and electron

transport layer), which simplifies the preparation process and makes it more convenient for low-temperature fabrication. To date, the best n-i-p planar devices have efficiencies around 19% with different electron transport layers (TiO_2, SnO_2 etc.).[11, 46, 47] Recently, the p-i-n planar devices have also demonstrated efficiencies higher than 18% due to the employments of advance film preparation methods.[39, 40, 48-50]

1.3 Two-dimensional materials

2D materials have attracted tremendous interest in the research community since 2004, when Geim and Novoselov obtained single-layer graphene successfully by micromechanical cleavage from graphite.[51] These materials often consist of atomically thin sheets exhibiting strong in-plane covalent bonding and weak out-of-plane van der Waals interactions. Therefore, they can be exfoliated into freestanding monolayer or few-layer thin flakes, which have a variety of distinctive and extraordinary optoelectronic properties. Here, we just give a brief introduction of some mostly often studied 2D materials as well as the synthesis methods.

1.3.1 Categories of 2D materials

Graphene and its derivatives

Graphene, an atomically thin carbon layer with a two-dimensional honeycomb hexagonal lattice, is the first extensively investigated 2D material. It is the basic allotrope of all the other forms of carbon materials, like graphite, carbon nanotubes (CNTs) and fullerenes.[52] Graphene exhibits many exceptional properties. It has high carrier mobility[53], high electrical conductivity (zero-bandgap semimetal)[54], high mechanical strength (the strongest material ever measured)[55], high optical transparency[56], wide light response range[57], high thermal conductivity[58], large specific surface area[59], low cost, robust chemical stability, tunable band gap[60] etc., all of which make it highly attractive for numerous applications. The pristine graphene material is hydrophobic, and it cannot be well dispersed in water. However, after oxidization through the mostly often used Hummer's method[61] (by treatment with

strong acids and oxidizing agents), the so-called graphene oxide (GO), an important derivative of graphene, can be obtained and dispersed uniformly in aqueous solution due to the introduction of many functional groups during the preparation process. That's because these attached functional groups (like epoxide, carbonyl and hydroxyl groups) on the graphene surface or edges are mainly hydrophilic. This allows the large-scale production of GO solution as well as large area uniform films with high yield, which is beneficial for commercial applications. In contrast to graphene, the as-synthesized GO is insulating with poor electrical conductivity, but it can be transformed into reduced graphene oxide (rGO) with high conductivity and transparency after chemical reduction processes.[62, 63] Although the graphene structure in rGO cannot be fully restored (with many residual defects)[64], the facile solution processability of rGO enables the easy preparation of conductive films or contacts in low temperature. Apart from GO and rGO, some other derivatives of graphene, such as graphene quantum dots (GQDs) and graphene nanoribbons, have also been widely studied and applied in various research area.

Transitional metal dichalcogenides

Transition metal dichalcogenides (TMDs) are another large group of 2D materials with a general formula of MX_2, where M is transition metal atom (Mo, W, etc.) and X represents chalcogen atom (S, Se, or Te).[65] The metal atoms in monolayer TMDs are sandwiched between two layers of chalcogen atoms via covalent M-X bonding, while adjacent layers of TMDs (in bulk forms) are coupled by weak van der Waals forces, enabling exfoliation into single layers. Unlike the bulk counterparts with indirect bandgaps, 2D monolayers of TMD materials have a direct bandgap. Thus, TMDs such as MoS_2 and WS_2, have tunable bandgaps with layer-dependent properties.[66] TMDs has been very attractive due to their tunable electronic structures and solution processability. So far, significant progress has been made in many application areas of the 2D TMDs materials.[67]

Hexagonal boron nitride

Monolayer hexagonal boron nitride (*h*-BN) is comprised of alternating boron and nitrogen atoms with a honeycomb lattice arrangement, sharing a similar lattice structure with graphene.[68] *h*-BN has a wide band gap of around 6 eV.[69] Its insulating property, atomically smooth surface, and superb chemical stability, make it an appealing substrate or dielectric layer for the fabrication of many electronic devices.[70]

Black phosphorus

Black phosphorus (BP) is one of the allotropes of phosphorus. BP, with a puckered orthorhombic layered structure, has recently emerged as a promising two-dimensional semiconducting material owing to its extraordinary electronic properties, like tunable direct bandgap and high carrier mobilities.[71] A high room-temperature hole mobility of 5200 $cm^2V^{-1}s^{-1}$ was obtained by Long *et al*. from a field-effect transistor made of few-layer BP.[72] Unlike the zero band gap of graphene, BP has a thickness-dependent band gap, which can be tuned from a narrow band gap of around 0.3 eV (for bulk BP) to a large band gap value around 2 eV (for single-layer). And unlike MoS_2 which has a direct band gap only in its monolayer form (with indirect band gap in the bulk), BP has a universal direct bandgap.[71, 73] Therefore, BP material bridges the energy gap between graphene (zero-bandgap) and TMDs (with large bandgaps), making BP material an ideal candidate for various near and mid-infrared optoelectronic applications.[74] Its excellent electronic properties make it an attractive nanomaterial with vast applications.

1.3.2 Synthesis of 2D materials

The mostly often used methods for the preparation of 2D materials include exfoliation methods and chemical vapor deposition (CVD) methods.[75] Mechanical exfoliation by scotch tape was firstly used for obtaining of the graphene flakes from bulk graphite crystals in 2004.[51] Through repeated sticking and peeling of bulk crystals (with layered structure) by using scotch tape, single or few-layer nano-flakes can be obtained. 2D flakes prepared by mechanical exfoliation normally have high crystallinity and low density of traps, which are suitable for fundamental investigations. However, it is difficult for the precise control of the flake size and thickness, and it is not suitable for

large-scale applications. For mass-production purpose, solution-based exfoliation methods are often used to disperse 2D materials into various solvents by chemical or ultrasonication approaches.[75, 76] The solvent molecules can interpenetrate into the layers of 2D materials with the help of chemical reaction and sonication processes. The resulting dispersion can be deposited on various substrates conveniently for film preparation. Compared with mechanical exfoliation, solution-based exfoliation methods provide the possibility of 2D material preparing in relatively large quantities for commercial applications.

Although highly crystalline 2D materials can be prepared with mechanical exfoliation method and all kinds of solution-based methods can fulfill the requirements of mass-production, it is difficult to get high-quality, large-area and continuous monolayer or few-layer films of 2D materials, unless using the so-called CVD method. For example, large-area single- or few-layer graphene films can be grown on copper foils with CVD method based on a surface-catalyzed process.[77] In typical CVD processes, the substrates (normally are metal substrates like Ni, Cu, Pt) are exposed to the vapor of precursor materials, which react and/or decompose on the substrate surface to produce the desired films. In many cases, the grown films of 2D materials need to be transferred to some other substrates for various applications by using wet-transfer or dry-transfer approaches. 2D materials grown by CVD methods can have better morphological and optoelectronic properties than that of the solution-based 2D materials.[52]

1.4 Applications of 2D materials in PSCs

Currently, 2D materials have been widely investigated for a wide range of electronics and optoelectronics applications, including field-effect transistors[51, 78-81], photodetectors[82-86], solar cells[75, 87-91], light-emitting diodes[92], lithium ion batteries[93, 94], photocatalysis[95], flexible electronics[96], biosensors[97-100], supercapacitors[59], optical modulators[101] and so on. Recently, applications by combining the outstanding properties of 2D materials and organic-inorganic hybrid perovskite materials have been revealed for the fabrication of high-performance PSCs with impressive operational

stability. The conducting graphene films have been used as contact materials to replace the traditional transparent conductive oxides or metal electrodes. Graphene and its derivatives, TMDs, BP and some other 2D materials have been employed for hole transporting and electron transporting or simply incorporated in the perovskite layer.

2. Graphene-based materials as electrodes

Due to the low temperature processing feature of graphene films as well as their high conductivities and outstanding mechanical properties, graphene electrodes can be utilized to replace the traditional transparent conductive oxides (indium-doped tin oxide (ITO) or fluorine-doped tin oxide (FTO)) to prepare flexible PSCs with extraordinary flexibility. Similarly, in view of the high transparency of the single atomic thick graphene films, they can be used as excellent transparent electrodes to realize highly-efficient semitransparent PSCs, which have broad applications in building integrated photovoltaics (BIPVs) and tandem solar cells. This part summarized the published work of using graphene-based materials as bottom and top electrodes, as listed in Table 1.

2.1 Bottom electrodes

2.1.1 Normal structure PSCs

CVD synthesized graphene films can be used as transparent bottom electrodes in normal structure PSCs to replace the traditional conductive oxide electrodes (FTO or ITO), either on rigid substrates or on flexible substrates. Luo *et al*.[102] prepared all-carbon-electrode-based flexible PSCs with graphene as bottom electrode and carbon nanotubes (CNTs) as top electrode. The PSCs with a configuration of FET/graphene/TiO_2/PCBM/$MAPbI_3$/spiro-OMeTAD/CNTs achieve a PCE of 11.9%, while a PCE of 8.4% can be obtained when spiro-OMeTAD was omitted. Fig. 2a shows the device structure of the all-carbon-electrode-based flexible PSCs. The freestanding CNT electrodes (with sheet resistance of ~ 41 Ω sq^{-1}) used here were cross-stacked from highly super-aligned CNT arrays prepared by a CVD method, while the transparent graphene electrodes were fabricated by transferring CVD graphene onto PET substrate.

The effect of layer number of graphene electrodes was studied, and the current density-voltage (*J-V*) curves of the best performing devices were shown in Fig. 2b. It was found that the conductivity of the graphene electrodes increased with the increase of the layer number, while the transparency decreased. Therefore, the devices with 2-layer graphene electrodes had the highest PCE of 11.9%, which was actually a tradeoff between the sheet resistance and transparency of the multi-layer graphene electrodes. It was noted that the hole transport layer free devices (without spiro-OMeTAD) also demonstrated relatively good efficiency (8.4%), which shows that the all-carbon electrodes have great potential in the application of hole transport layer free PSCs. The bending stability of the flexible devices were tested for different bending cycles at various curvature radius. For comparison of the mechanical properties, the PSCs with ITO and Au electrodes (with a structure of FEN/ITO/TiO_2/PCBM/$MAPbI_3$/spiro-OMeTAD/Au) were also prepared as control devices. For the bending test at a curvature radius of 4 mm, the control devices degraded to 87% of the original efficiency after 200 bending cycles, while the efficiency of the flexible all-carbon-based devices had no obvious degradation. Once the curvature radius was decreased to 2.2 mm, the control devices were almost completely damaged due to the conductivity loss of the ITO electrodes after deformation, while the all-carbon-electrode-based PSCs could still attain 85% of the initial value. For further bending test at more bending cycles (2000 times), the efficiencies of the all-carbon-electrode-based PSCs and control devices suffered 16% and 87% of the original value, respectively. It was found that the sheet resistance of the PET/graphene and CNTs electrodes was almost unchanged after bending test of 2000 cycles (at bending curvature of 4 mm), while the electrical resistance of the PEN/ITO electrode increased for about 12 times of the original value, showing the much better mechanical properties of the graphene and CNTs electrodes during bending test. Besides, the photostability and thermal stability of the carbon-based and ITO-based PSCs were also studied in ambient air. The results indicated that the all-carbon-electrode-based PSCs performed significantly better stability than the control devices (with metal top electrodes), maintaining 92% of the original efficiency after light soaking of about 1000 h (AM 1.5G irradiation) and 89% of the initial value after

thermal test of more than 1500 h (60ºC in dark). The improved device stability should be ascribed to two reasons. First, the carbon-based electrodes will not diffuse into the perovskite layer or react with it, because of the robust chemical stability of carbon materials, while the metal electrodes in the control devices tend to diffuse into the perovskite layer and irreversible damage can be generated.[103, 104] Second, the thick (1.2-μm thick) and hydrophobic CNTs top electrode can also work as a good barrier layer to protect the underlying perovskite layer from the moisture in air. This was confirmed by the XRD characterization of the perovskite layers after PSCs were exposed in air (humidity ~ 70%) for 300 h. A strong diffraction peak of PbI_2 in the XRD pattern was observed in the Au-based control devices, while it was not found in the carbon-based PSCs, indicating the outstanding protecting effect of the CNTs electrodes. Meng *et al*.[105] also demonstrated the utilization of CVD graphene as bottom electrodes in normal structure PSC, as shown in Fig. 2c-d. The PSC was also all-carbon-electrode-based with a device structure of quartz/graphene/C_{60}/$MAPbI_3$/carbon. An efficiency of 13.93% was obtained from the reverse scan of the *J-V* curves. However, the FF of the device is relatively low (59.1%), which should be attributed to the high sheet resistance (~ 400 Ω sq^{-1}) of the monolayer graphene film on quartz substrate. Therefore, the conductivity and quality of the transferred graphene films can severely impact the device performance.

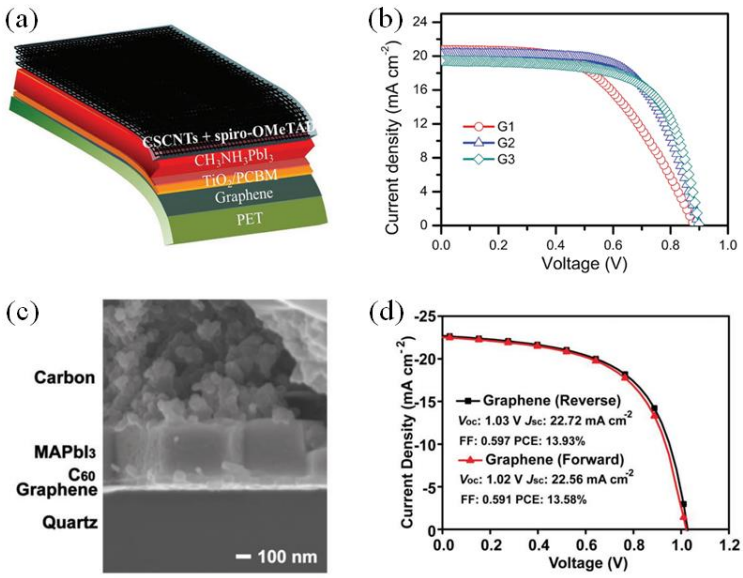

Fig. 2. All-Carbon-Electrode-Based PSCs with graphene as bottom electrodes. Device structure (a)

and *J-V* characteristics of the flexible all-carbon-electrode-based PSC with graphene as bottom electrode. Reproduced with permission from ref. [102]. Cross-sectional SEM image (c) and *J-V* curves (d) of the all-carbon-electrode-based PSC on quartz substrate with graphene as bottom electrode. Reproduced with permission from ref. [105].

In general, there are mainly two processes for the preparing of graphene transparent electrodes, including transferring of CVD graphene (grown on metal substrates) and solution processed graphene. Compared with CVD graphene, solution processed graphene electrodes can have lots of advantages, such as low cost, low temperature, easy fabrication and suitable for large-scale production. Batmunkh *et al*.[106] reported the utilization of solution processed transparent conductive rGO films as bottom electrodes in mesoporous PSCs with a device structure of glass/rGO/c-TiO_2/mp-TiO_2/$MAPbI_3$/spiro-OMeTAD/Au. The rGO films prepared through a vacuum-filtration and transfer technique show high sheet resistance (~ 3 KΩ sq-1) and low optical transmittance (~55%). Therefore, the PSCs with this rGO bottom electrodes show a low PCE of 0.62%. Similarly, Liu *et al*. [107] also fabricated planar PSCs (glass/rGO/TiO_2/$CH_3NH_3PbI_3$/spiro-OMeTAD/Au) with graphene electrodes prepared by solution printing method. Both spray coating and blade coating were used to make the graphene films. A promising PCE of 3.38% was achieved, indicating that the solution printing method has great potential as an approach for large-scale production of graphene films, although the conductivities of these films need to be greatly improved.

2.1.2 Inverted structure PSCs

In 2015, Sung *et al*.[108] first reported the adoption of graphene as bottom electrodes in inverted structure PSCs, which have a configuration of glass/graphene/MoO_3/PEDOT:PSS/$MAPbI_3$/C_{60}/BCP/LiF/Al, as shown in Fig. 3a-b. The single layer CVD graphene films prepared through a typical wet transfer process were used as transparent anode. Because of the hydrophobic nature of graphene films, it is difficult to deposit high quality PEDOT:PSS films on top of graphene films. Moreover, the conductivity of the pristine monolayer graphene film is not high enough

for the application as transparent electrodes. To tackle these problems, an ultrathin MoO_3 layer (1 ~ 4 nm) was deposited on graphene surface by vacuum thermal evaporation. As shown in Fig. 3c, the contact angles of PEDOT:PSS aqueous solution on graphene surfaces decreased dramatically from 90.4º to 46.6º after deposition of a 1-nm thick MoO_3 layer, and further reduced to 30.0º when the thickness of MoO_3 layer increased to 2 nm, which can help improve the quality of PEDOT:PSS film formed on top of graphene films. Besides, it is surprising to find that the sheet resistance of the as-prepared graphene films (> 2000 Ω/□) dropped to ~ 800 Ω/□ just because of the p-type doping effect of the 0.5-nm thick MoO_3 layer. This value further decreased to ~ 500 Ω/□ when 2 nm MoO_3 layer was deposited, as shown in Fig. 3c. Moreover, the ultraviolet photoelectron spectroscopy (UPS) data also indicated that the work function of graphene film increased from 4.29 eV to 4.65 eV after MoO_3 modification (as shown in Fig. 3b), which reduced the energy barrier at the interface between PEODT:PSS layer and graphene electrodes, favoring more efficient hole collection. As a result, a champion efficiency of 17.1% was achieved with MoO_3 thickness of 2 nm. This efficiency was comparable with that of the reference devices on ITO substrates (without MoO_3). Although the conductivity of the graphene films was improved after MoO_3 modification, the sheet resistance of graphene electrodes (~ 500 Ω/□) was still much higher than that of ITO glass (~ 9.5 Ω/□). Thus, the FF of the graphene-based PSCs was inferior to that of the control devices due to the higher series resistance and lower shunt resistance. However, it was noteworthy that their short circuit currents were of similar values despite of the difference in conductivities, which should be due to the higher transparency of the graphene film (~97%) than that of ITO electrodes (~89%). The low charge conducting ability of single layer graphene film was compensated by its better optical transparency. Besides, the V_{oc} of the graphene-based device (~1.03 V) was also higher than that of the control devices (0.96 V), which was attributed to the increased work function of the MoO_3-modified graphene electrodes.

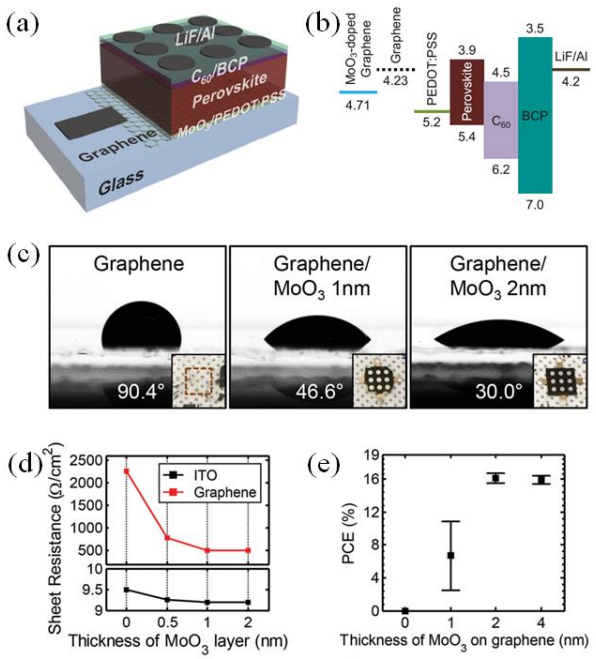

Fig. 3. Schematic structure (a) and corresponding energy level diagram (b) of the inverted PSCs with graphene as transparent bottom electrodes (anode). (c) Contact angles of PEDOT:PSS aqueous solution on graphene and MoO_3-modified graphene films. (d) The relationship between MoO_3 layer thickness and the sheet resistance of graphene and ITO electrodes. (e) The PCEs of PSCs with graphene electrodes as a function of MoO_3 layer thickness. Reproduced with permission from ref. [108].

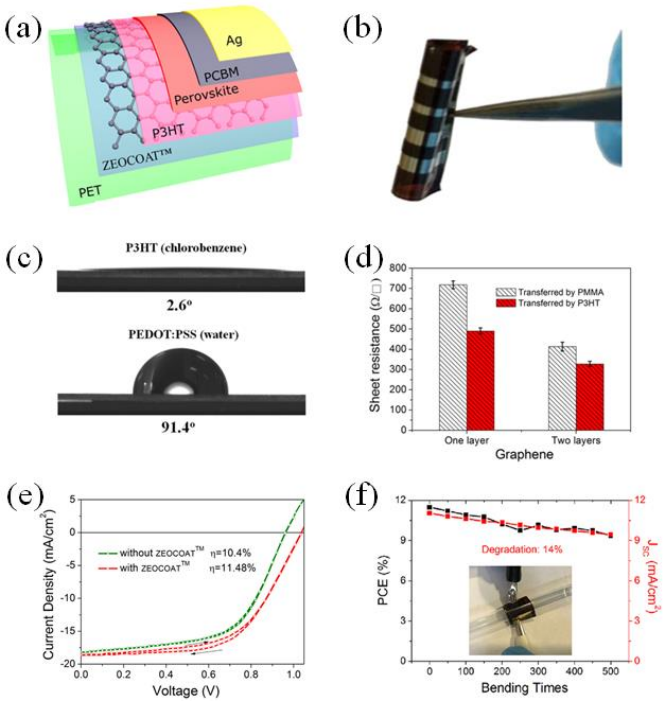

Fig. 4. Schematic diagram (a) and photograph (b) of the flexible PSC on ultrathin PET substrate with CVD graphene as bottom electrode. (c) Comparison of the contact angles when P3HT solution (dissolved in chlorobenzene) or PEDOT:PSS aqueous solution were dropped onto the graphene films. (d) The sheet resistance of graphene films (single layer or double layer) transferred by PMMA

or P3HT. (e) *J-V* curves of the flexible PSCs with or without ZEOCOAT modification of the PET substrates. (f) The bending stability of the flexible PSC at a bending radius of 0.175 cm. Inset shows the photograph of the devices attached on the curved surface for bending tests. Reproduced with permission from ref. [109].

In terms of wearable photovoltaics, it is difficult to get highly flexible solar cells with the traditional ITO electrodes because of their brittle nature. However, the robust mechanical properties of graphene electrodes make it possible to fabricate ultra-flexible PSCs. In 2016, Liu *et al*.[109] demonstrated the successful fabrication of flexible PSCs with graphene as bottom electrodes for the first time. The flexible PSCs possessed a novel device structure of PET/ZEOCOAT/graphene/P3HT/$MAPbI_3$/$PC_{71}BM$/Ag, as shown in Fig. 4a-b. Double layer graphene films were transferred to ultra-thin PET substrates (with a thickness of 20 μm) and used as anodes. Because the PET substrates were relatively rough, a layer of cross-linkable olefin-type polymer (ZEOCOAT™) was used as interlayer between PET substrate and graphene film to reduce the surface roughness, which was confirmed to be able to increase the device efficiency, as shown in Fig. 4e. Double layer graphene films were employed here because of their better conductivity compared with the single layer graphene and the reasonable transparency in the visible range (~ 90%, much higher than that of ITO).[88, 110, 111] Especially, the CVD graphene films on copper substrates were transferred by poly(3-hexylthiophene-2,5-diyl) regioregular (P3HT) instead of the traditional Poly(methyl methacrylate) (PMMA) material. As a result, graphene films with better conductivity and cleaner surfaces and edges were obtained, because the P3HT is much easier to be removed after transformation than PMMA, and the graphene film was doped by P3HT (p-type doping) to have lower sheet resistance, as shown in Fig. 4d. The p-type doping effect of P3HT here is quite similar with that of the ultrathin layer of MoO_3 on graphene films as discussed above.[108] From the point of device structure design, it is very important to have clean graphene edges when the active area of the solar cell is defined by the overlap part between the graphene bottom electrode and the rectangular metal top electrode, unlike the design in Fig. 3a, where small circular metal top electrodes were deposited, and the cells must be tested with the assistance of conducting probes, which

is not suitable for real applications. As for the hole transport layer in the solar cells, P3HT was utilized to replace the traditional PEDOT:PSS material. P3HT shows several advantages over PEDOT:PSS. Firstly, the chlorobenzene solution of P3HT shows extremely lower contact angle on graphene surface than that of PEDOT:PSS aqueous solution, as shown in Fig. 4c, leading to better coverage of the hole transport layer. Secondly, the PSCs with P3HT as hole transport layer turned out to be much more stable than that with PEDOT:PSS, because P3HT is hydrophobic while PEDOT:PSS tend to absorb moisture in air. Owing to the above novel advancements in the device structure, the ultra-flexible graphene-based PSCs achieved a PCE of 11.5%, which only degraded for ~ 14% after 500 bending cycles at a bending radius of 1.75 mm, demonstrating a good bending durability, as shown in Fig. 4f. It was considered that the degradation was originated from the cracking of perovskite films under mechanical stress during the bending process. Besides, by comparing the 20-μm thick PET with the 200-μm thick PET, it was found that the PSCs prepared on 20-μm PET substrates appeared to have much better bending stability and a higher specific weight (5 W/g). Therefore, choosing thinner flexible substrates should be a feasible way to enhance the flexibility of flexible optoelectronic devices. Later in 2016, Yoon *et al*.[112] reported super-flexible PSCs with a champion efficiency of 16.8% by using MoO_3-modified single-layer CVD graphene as bottom electrodes, which was based on their previous work on glass substrates[108]. The flexible PSC had a device structure of PEN/graphene/MoO_3/PEDOT:PSS/$MAPbI_3$/C_{60}/BCP/LiF/Al. The graphene-based flexible PSCs can maintain over 90% of the original efficiencies after bending test of 1000 cycles at a bending radius of 2 mm, while the efficiencies of the control devices prepared on flexible ITO electrodes decreased to less than 40% of the initial values. Even after 5000 bending cycles, the graphene-based flexible PSCs can still retain 85% of the original efficiency, showing excellent bending stability.

In order to attain higher efficiencies of the graphene-based PSCs, how to further reduce the sheet resistance of the graphene films is a key problem. Im and coworkers employed $AuCl_3$-doped graphene[113] and bis(trifluoromethanesulfonyl)-amide (TFSA)-doped

graphene[114] as bottom electrodes for super-flexible PSCs. After highly p-type chemical doping with $AuCl_3$ or TFSA, the sheet resistance of single layer graphene film decreased significantly to approximately 100 Ω/□, which is much lower than the above-mentioned values for monolayer graphene, as shown in Table 1. An APTES (3-aminopropyl triethoxysilane) inter-layer was inserted between the flexible substrate and the graphene film to promote the adhesion of graphene, which contributed a lot to the better bending durability of the PSCs. Besides, the perovskite material $FAPbI_{3-x}Br_x$ was used for wider light absorption. As a result, ultra-flexible PSCs with high PCEs (around 18%) and excellent bending durability were obtained.

2.2 Top electrodes

In terms of the selection of the top electrode materials for solar cells, researchers have been looking for alternatives of the traditional noble metal materials (such as Au, Ag). For example, carbon materials (including carbon black, carbon nanotubes and graphene)[87, 88, 110, 115-122], metal nanowires (e.g. silver nanowires)[123-125] and conductive polymers (e.g. PEDOT:PSS)[126, 127] have been utilized as top electrodes. Among these materials, graphene has been considered one of the best candidates due to its low-cost and superb optoelectronic properties, especially for the application of semitransparent solar cells. You *et al*.[110] reported the implementation of graphene top electrodes in PSCs for the first time in 2015. As shown in Fig. 5a-b, the device had a configuration of glass/FTO/TiO_2/$MAPbI_{3-x}Cl_x$/spiro-OMeTAD/PEDOT:PSS/graphene/PMMA/PDMS. The perovskite major part (glass/FTO/TiO_2/$MAPbI_{3-x}Cl_x$/spiro-OMeTAD) and the transparent graphene electrode part (PDMS/PMMA/graphene) were prepared separately, and then laminated together under appropriate pressure to get the final device. CVD graphene was used for top electrodes after the typical wet-transfer process with PMMA. It was noted that Polydimethylsiloxane (PDMS) was used as a support for the PMMA/graphene film. Since both the bottom electrode (FTO) and top electrode (graphene) in the device were highly transparent, the final cells were semitransparent and can absorb light from both sides. The sheet resistance of the single layer graphene electrode (~ 1050 Ω sq^{-1})

decreased to about 260 Ω sq^{-1} after spin-coating of a PEDOT:PSS layer (PH500 with Zonyl FS-300 and D-sorbitol as additives). Zonyl FS-300 (1 wt%) was used as surfactant in the PEDOT:PSS aqueous solution to reduce the contact angle on graphene films, while D-sorbitol was introduced to increase the adhesiveness of the PEDOT:PSS film to achieve a better contact between the graphene electrode and the spiro-OMeTAD film. The PSCs with D-sorbitol introduction (150 mg/ml) demonstrated 3 times higher PCEs than that without D-sorbitol. Thus, the PEDOT:PSS/D-sorbitol composite was confirmed to be an excellent electronic glue for laminated electronic devices. To further increase the conductivity of the graphene top electrodes, multilayer graphene electrodes were prepared. The PEDOT:PSS-coated 2-layer graphene electrodes showed a low sheet resistance of ~ 140 Ω sq^{-1} while still maintaining transmittances over 90% in the visible light range. The effect of layer number of graphene electrodes was investigated as shown in Fig. 5c-d. The devices with single-layer graphene electrodes had the worst performance because of the bad conductivity of the single-layer graphene film, while the PSCs with 2-layer graphene electrodes achieved the champion efficiency of 12.37% and 12.03% when light was illuminated from FTO and graphene sides, respectively. However, the performances of devices with 3 or 4 layers of graphene electrodes were inferior to that of devices with 2-layer graphene electrodes, which should be originated from the rough graphene surfaces with lots of wrinkles introduced during the layer-by-layer stacking process. To improve the device transparency, graphene-based semitransparent PSCs with different perovskite layer thickness (150~350 nm) were fabricated and characterized, as shown in Fig. 5e-f. It was reasonable to find that the device efficiencies decreased with the increase of the perovskite layer thickness, and those PCE values were relatively high compared with other reports of semitransparent solar cells at the same device transparency. Therefore, the CVD graphene electrodes were quite promising as an alternative to the traditional Au electrodes, especially for the applications of efficient semitransparent PSCs.

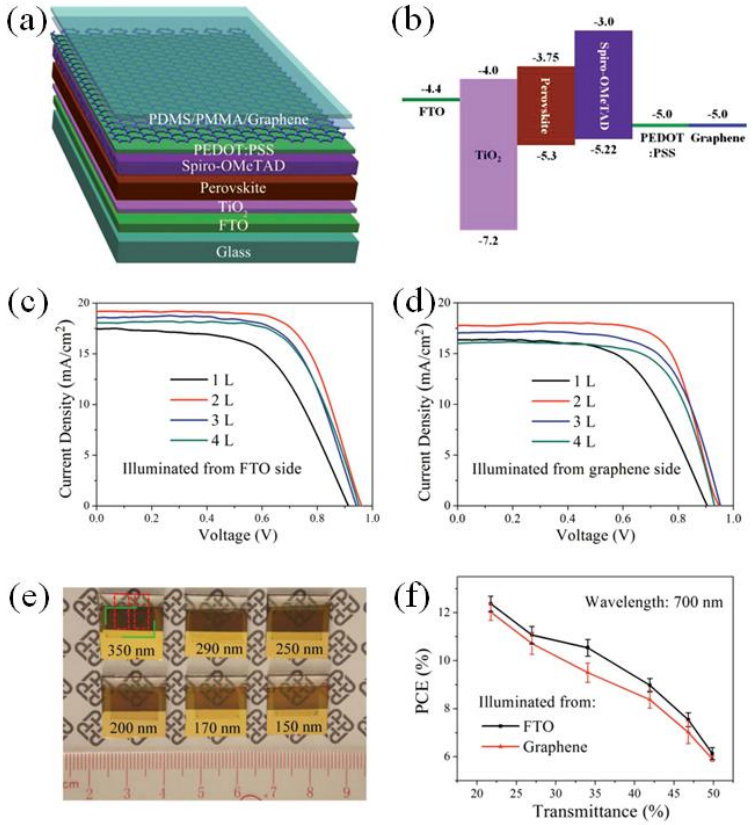

Fig. 5. The schematic diagram (a) and energy band diagram (b) of the semitransparent PSC with graphene top electrode. (c,d) The *J-V* curves of the semitransparent PSCs consisting of different graphene layers (1~4 layers) when light was illuminated from two opposite sides. (e,f) The photograph and PCEs of graphene-based semitransparent PSCs with different transparencies. Reproduced with permission from ref.[110].

Semitransparent PSCs have been demonstrated to have great potential for the applications in tandem solar cells by integrating PSCs with silicon, CIGS, DSSCs, organic solar cells or even PSCs.[128-132] The tunable bandgaps of the organic-inorganic hybrid perovskite materials together with the highly transparent property of graphene electrodes make the graphene-electrode-based semitransparent PSC one of the ideal top cells (with wide bandgaps) for tandem solar cells. Lang *et al*.[118] implemented large-area CVD graphene films to obtain semitransparent PSCs (PCE~6.2%), and then combined them with a bottom silicon cells (PCE~7.0%, after filtered by top cells), achieving a champion PCE of 13.2% in the final tandem cells. Besides, following the method used in the previous report (semitransparent PSC with laminated graphene top electrodes)[110], Zhou *et al*.[119] successfully fabricated 4-terminal perovskite/Si tandem

solar cells with a high efficiency of 18.1% (the PCEs of the top perovskite cell and the bottom Si cell were 11.8% and 6.3%, respectively), demonstrating the great potential of graphene electrodes for tandem solar cell applications. However, further developments of the quality of the transferred graphene electrodes as well as the configuration design of the tandem cells are needed to take full advantage of the graphene material and get higher PCEs. Also, it is challenging to realize 2-termainal tandem cells with graphene electrodes.

In addition to the above introduction, the graphene materials have also been utilized as top electrodes for hole transport layer free (HTL-free) PSCs. Due to the high cost of the novel metal electrodes (Au, Ag etc.) and HTL materials (spiro-OMeTAD, PTAA etc.) used in typical PSCs, considerate efforts have been devoted to developing HTL-free PSCs with low-cost carbon-based contact materials, such as carbon black, graphite, graphene and CNTs.[115, 117, 133] These PSCs are generally much more stable in ambient air than those with organic HTLs and metal electrodes. Recently, graphene films synthesized by different approaches have been successfully adopted as counter electrodes for HTL-free PSCs.[120-122] Yan *et al*.[120] reported the implementation of the chemically reduced graphene oxide as top electrodes of HTL-free PSCs with a device structure of FTO/TiO_2/$MAPbI_3$/graphene. Both single-layered graphene (SG) and multilayered graphene (MG) used in the work were synthesized through the reduction of their oxides (SGO and MGO), which were chemically exfoliated from the natural graphite crystals. The Fermi levels of SG and MG films were determined to be -4.8 eV and -5.0 eV respectively by UPS measurements. Therefore, MG formed Schottky junction with perovskite (Fermi level ~ -4.73 eV), while SG had ohmic contact with perovskite. As a result, the PSCs with MG electrodes showed higher PCE (11.5%) than that of devices with SG electrodes (6.7%), demonstrating the essential effect of the Schottky barrier which enhanced the hole extraction and electron blocking in the HTL-free PSCs. Zhu *et al*.[121] employed fumaric acid, Na_2CO_3 and urea as raw materials to synthesize nitrogen doped graphene frameworks (N-doped GFs) through a fast pyrolysis process at high temperature (1000ºC) under a flow of argon atmosphere. The

N-doped GFs were utilized as excellent top electrodes for HTL-free PSCs, and a PCE of 10.32% was achieved. Wei *et al*.[122] synthesized 3D honeycomb-like graphene sheets by chemical reaction between Potassium and CO_2. Those graphene sheets exhibited excellent performance when used as counter electrodes for HTL-free PSCs with a PCE of 10.06%. It is notable that the above HTL-free PSCs were normally prepared by drop-casting of the reactive paste of graphene and CH_3NH_3I (dispersed in 2-propanol) onto the FTO/TiO_2/PbI_2 film. After subsequent thermal annealing, the perovskite films were well crystallized. This special 2-step process could ensure good contact between the perovskite layer and the graphene top electrode, thereby yielding perfect hole extraction. Therefore, the graphene-based counter electrodes provide a simple but effective solution to the cost reduction and long-term stability enhancement of PSCs, facilitating their commercialization process.

Table 1. Summary of the PSCs with graphene electrodes.

Electrode material	Sheet resistance (Ω sq^{-1})	Transmittance at 550 nm (%)	Electrode location	Device structures	PCE (%)	Ref.
CVD graphene	290	87.3	Bottom	FET/Graphene/TiO_2/PCBM/$MAPbI_3$/Spiro-OMeTAD/CNTs	11.9	[102]
CVD graphene	400	~ 90	Bottom	quartz/graphene/C_{60}/$MAPbI_3$/carbon	13.93	[105]
Solution processed rGO	3080	55	Bottom	Glass/rGO/c-TiO_2/ mp-TiO_2/$MAPbI_3$/Spiro-OMeTAD/Au	0.62	[106]
Solution processed rGO	3400	75	Bottom	Glass/rGO/TiO_2/$MAPbI_3$/Spiro-OMeTAD/Au	3.38	[107]
CVD graphene (1 layer)	500	97	Bottom	Glass/graphene/MoO_3/PEDOT:PSS/$MAPbI_3$/C_{60}/BCP/LiF/Al	17.1	[108]
CVD graphene (2 layers)	~330	~90	Bottom	PET/ZEOCOAT/graphene/P3HT/$MAPbI_3$/$PC_{71}BM$/Ag	11.5	[109]
CVD graphene (1 layer)	~550	~97	Bottom	PEN/graphene/MoO_3/PEDOT:PSS/$MAPbI_3$/C_{60}/BCP/LiF/Al	16.8	[112]
CVD graphene (2 layers)	~470	~95	Bottom	PET/graphene/PEDOT:PSS/$MAPbI_3$/PCBM/Al	13.94	[111]
CVD graphene (1 layer)	~80	-	Bottom	PET/graphene/PEDOT:PSS/$FAPbI_{3-x}Br_x$/PCBM/Al	17.9	[113]
CVD graphene (1 layer)	~116	96.8	Bottom	Glass or PDMS/graphene/PEDOT:PSS/$FAPbI_{3-x}Br_x$/PCBM/Al	18.3	[114]
CVD graphene (2 layers)	~140	~91	Top	FTO/TiO_2/$MAPbI_{3-x}Cl_x$/Spiro-OMeTAD/PEDOT:PSS/graphene	12.37	[110]
CVD graphene (1 layer)	-	-	Top	FTO/TiO_2/$MAPbI_3$/Spiro-OMeTAD/graphene	6.2	[118]

CVD graphene (2 layers)	-	82.5	Top	FTO/TiO_2/$MAPbI_{3-x}Cl_x$/Spiro-OMeTAD/PEDOT:PSS/graphene	11.8	[119]
Solution processed rGO	-	-	Top	FTO/TiO_2/$MAPbI_3$/graphene	11.5	[120]
Pyrolyzed graphene frameworks from fumaric acid	-	-	Top	FTO/TiO_2/$MAPbI_3$/graphene	10.32	[121]
Potassium-chemically synthesized 3D graphene from CO_2	~3970	-	Top	FTO/TiO_2/$MAPbI_3$/graphene	10.06	[122]

3. 2D materials for hole transporting

In perovskite solar cells, the charge transporting layers (CTLs) are of great importance for the photovoltaic performance and long-term stability[11, 134]. Generally, the superior CTLs should have several requirements in optical and electric properties. First, the band energy structure of CTLs should match with that of perovskite absorber to extract the holes and electrons and transport them to the corresponding electrodes efficiently. Besides, the better energy match could reduce the loss in potential and obtain higher open-circuit voltage in the photovoltaic performance[11]. Second, the charge carrier mobility of CTLs is crucial for the photovoltaic performance of PSCs. The CTLs with high hole (electron) mobility could transport holes (electrons) efficiently and reduce the recombination with the electrons (holes) significantly. Third, in terms of long-term stability, the CTL materials could not have chemical reaction with the perovskites [135]. In addition, the perovskite would decompose in the humid atmosphere. Thus, the CTLs with hydrophobicity are favorable to protect the perovskite from the infiltration of water. In the last, for the CTLs serving as the growth substrates for the perovskite, the surface property, such as wettability and smoothness, play crucial roles in the quality of the fabricated perovskite films.[136] Moreover, high optical transmittance of the CTLs is required to reduce the loss of the incident light.

2D materials, such as graphene and TMDs, have been recognized as promising nanomaterials for future electronic and optoelectronic applications due to their unique properties such as high carrier mobilities, thickness-dependent band structure, ultra-

small thickness, smooth surface without dangling bonds and high compatibility with printable and flexible electronics [79, 82, 137-141]. Recently, many research works are focused on the exploration of 2D materials to improve the photovoltaic performance of PSCs due to their unique optoelectronic properties. In this part, we will comprehensively review the published work which employ 2D materials as hole transporting layers or dopants for the hole transporting layers to improve the photovoltaic performance and long-term stability, as summarized in Table 2.

3.1 Graphene and its derivatives

As the most famous 2D material, graphene has a mass of appealing mechanical, thermal, electronic and optoelectronic properties due to its novel structure of hexagonal honeycomb lattice [142]. The ultrahigh carrier mobility of over 10000 $cm^2V^{-1}s^{-1}$ enables graphene excellent carrier transporting material [137]. Graphene oxide, as the graphene derivative, is widely used in the solution processed devices due to its easy dispersibility in water and other organic solvents because of the presence of the oxygen functionalities. Recently, graphene and its derivatives are introduced into perovskite solar cells as hole transporting layer or dopants in the hole transporting layer to improve the photovoltaic performance.

3.1.1 Normal structure PSCs

In normal structure PSCs, the efficiency of PSCs employing spiro-OMeTAD as HTL have reached more than 22%[143]. In general, the p-type dopants, such as Li-bis (trifuoromethanesulfonyl) imide (Li-TFSI), are commonly used as dopants in spiro-OMeTAD to increase the conductivity and hole mobility and improve the photovoltaic performance of the devices. However, the dopants could accelerate the performance degradation of PSCs due to their deliquescent behavior [135]. Thus, some works are focusing on exploring graphene and its derivatives as HTL or dopants in HTLs to achieve stable and efficient PSCs.

Cao *et al*.[144] incorporated highly conductive graphene sheets into the self-synthesized hole transporting material, TSHBC (perthiolated trisulfur-annu-lated hexa-*peri*-

hexabenzocoronene), to increase the electrical conductivity. The shorter decay time of transient photoluminescence (PL) spectra (Fig. 6b) suggested that the introduction of graphene enhanced the hole transporting ability of TSHBC. The PCE was increased from 12.81% to 14.02% (Fig. 6a). The enhancement was mainly attributed to the increase of short-circuit current (J_{sc}), from 20.56 to 21.91 mA/cm^2, resulting from the improved conductivity of HTL by incorporating graphene sheets. Cogal *et al*.[145] demonstrated the fabrication of PSCs with the nanocomposite of graphene with PEDOT as HTL prepared by the radio frequency plasma method (Fig. 6c). This method is cost-effective, fast and environmentally friendly. The PSCs based on the iodine-doped composites achieved a PCE of 8.79% and retained about 72% of the initial PCE value after stored in the dark and humidity-controlled environment for 6 months (Fig. 6d). Ye *et al*. [146] used P3HT to replace the spiro-OMeTAD as hole transporting layer due to its low cost and easy of fabrication, as shown in Fig. 6e. The low hole mobility and conductivity of pristine P3HT layer lead to the low photovoltaic performance of PSCs[146]. The functional graphene (F-graphene) was introduced into the P3HT to increase the hole mobility and conductivity significantly. Moreover, the incorporation of F-graphene moved the work function value of P3HT from 5.0 to 5.2 eV, which facilitated the hole transfer at the interface between perovskite and P3HT (Fig. 6f). The efficiency was boosted from 8.16 to 13.82% by introducing 4% F-graphene into the P3HT layer. Due to the hydrophobicity of graphene composite, the 4 wt% F-graphene doped PSCs remained almost 70% of the initial PCE after storage in the ambient (temperature 25°C, humidity 20~40%) for 8 weeks, while the undoped P3HT devices left 35% of the original PCE. This suggests the high capacity of graphene in enhancing the PCE and stability of PSCs.

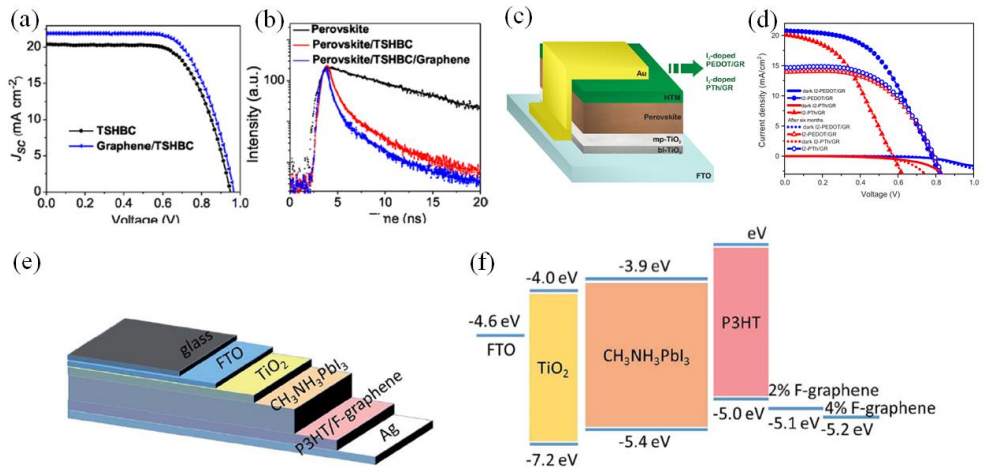

Fig. 6. (a) The champion *J-V* characteristics of PSCs. (b) Transient PL spectra of films. Reproduced with permission from ref.[144]. (c) Schematic illustration of the architecture and (d) *J-V* curves of PSCs fabricated with the novel HTMs I_2-doped PEDOT/GR and I_2-doped PTh/GR. Reproduced with permission from ref.[145]. (e) Schematic diagram of PSCs with P3HT HTL modified with F-graphene. (f) The schematic energy diagram of different layers in the PSCs. Reproduced with permission from ref.[146].

Wen *et al.*[147] proposed the employment of amino-functionalized graphene as an interlayer between perovskite and dopant-free spiro-OMeTAD layers to fabricate efficient perovskite solar cells. Due to coordinate or dative-covalent bond between amines on the graphene and the under-coordinated Pb^{2+} on the perovskite surface, the surface traps of the perovskite films were significantly reduced (Fig. 7a). Besides, the amino-functionalized graphene enhanced the hole extraction and transfer at the perovskite/HTL interface. Based on this interlayer, the PCE was increased from 10.70% to 14.60% (Fig. 7b). Luo *et al.*[148] proposed the employment of a highly conductive reduced graphene oxide treated by ferrous iodide acid solution, combined with undoped spiro-OMeTAD as a hole extraction and transport material in PSCs. The rGO was spin-coated between the perovskite and spiro-OMeTAD layers functioning as two roles :1) extracting the holes from perovskite layer and transporting them to the back electrode. 2) receiving the holes from spiro-OMeTAD and transporting them to the back electrode. Based on the enhanced hole transfer rate by using rGO, the maximum PCE of the fabricated devices was 10.6%, which is much higher than that of the devices using the dopant-free spiro-OMeTAD as HTL (6.5%). The stabilities were tested on the rGO-based devices and PSCs with Li-TFSI and pyridine doped spiro-OMeTAD stored in the

dark under ambient conditions (average temperature 20 ± 3 °C, humidity 40 ± 7%). The PCE of rGO-based PSCs remained above 85% of the original value after 500 h of storage. In contrast, the PCE of devices with doped spiro-OMeTAD was decreased to 35% of the initial value (Fig. 7c-d). The higher air stability is attributed to the hydrophobicity of rGO which protects the infiltration of water into perovskite layers.

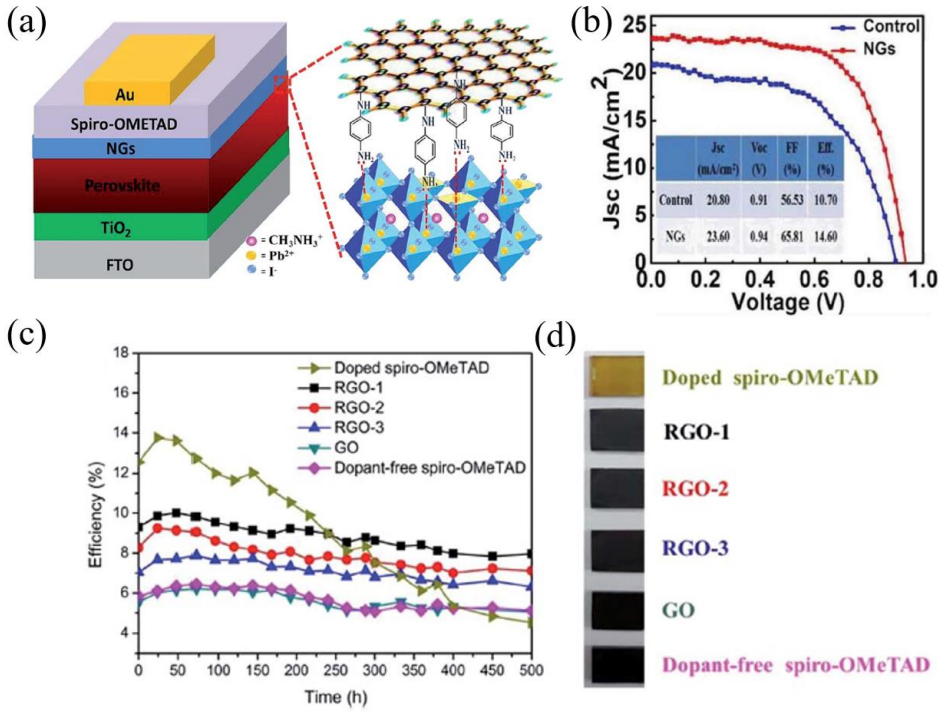

Fig. 7. (a) Schematic of PSCs with the amino-rich graphene interlayer. (b) The *J-V* characteristics of the champion PSCs under the illumination of one sun simulated solar light. Reproduced with permission from ref.[147]. (c) Efficiency stability of PSCs based on different hole transport layers. (d) Photo images of the protective effect of different hole transport layers on the surface of perovskite/TiO_2 film after 500 h storage in air. Films and cells without encapsulation were stored in air at room temperature and cells were measured under one sun solar irradiation. Reproduced with permission from ref.[148].

Yu *et al.* [149] exhibited the fabrication of highly efficient and stable normal structure PSCs by employing a water-free PEDOT and fluorinated graphene composite layer as HTL. The PCE of PSCs with the bilayer HTL reached 14.9%, which was much higher than that of the PSCs with single PEDOT HTL (10.3%). The comprehensive investigations suggested that the enhanced PCE of PSCs with the composite HTL was attributed to the alleviated charge recombination which was resulted from the interfacial dipoles at the PEDOT/rGO interface. These interfacial dipoles promoted the electron-

blocking and higher built-in potential in the devices. Moreover, due to the hydrophobicity of graphene sheet, the devices maintained 70% of the initial PCE after over 30 days exposure to ambient environment. Li *et al*.[150] prepared 4-fluorophenyl-hydrazine hydrochloride (4FPH) functionalized reduced graphene oxide (rGO-4FPH) as interlayer between perovskite and spiro-OMeTAD layers to passivate the surface traps of perovskite such as under-coordinated Pb ions and Pb clusters. The rGO-4FPH modified PSC achieved a PCE of 18.75% with a high V_{oc} of 1.11 V. For the reference device without rGO-4FPH, the PCE was 15.58% with a V_{oc} of 1.03 V. The increased V_{oc} was attributed to the deceased surface traps of perovskite resulted from the passivation of rGO-4FPH. Selvakumar *et al*.[151] used heteroatom doped reduced graphene oxide (B-rGO) papers to replace the spiro-OMeTAD as the HTL to prepare PSCs with the highest conversion efficiency of 8.96% and an active area of 1 cm^2. The B-rGO HTL paper was developed by the simple self-assembly process. This paper-like B-rGO HTL is more suitable for the fabrication of flexible photovoltaic devices. This work provides an effective protocol for fabricating simple, stable, low-cost and large area perovskite solar cells.

Li *et al*.[152] adopted graphene oxide as buffer layer between the perovskite and spiro-OMeTAD to enhance the interface contact and suppress the charge recombination at the interface. The enhanced interface contact led to the improved charge collection efficiency and led to the increase of J_{sc}. The suppressed charge recombination by the GO passivation resulted in the enhancement of V_{oc} and FF. The overall PCE was boosted from 10.0% to 15.1%. Nouri *et al*.[153] demonstrated the introduction of graphene oxide (GO) as buffer layer between perovskite and n-Butyl-substituted Copper Phthalocyanine (CuBuPc) layers to facility the hole extraction and avoid the formation of shunt paths towards both electrodes. With the insertion of GO, the PCE was increased from 7.3% to 14.4%. When Al_2O_3 was used as the buffer layer, the PCE was increased to 9.7%. The better effect of GO was ascribed to the excellent hole transfer property. For the spiro-OMeTAD and GO as HTL and buffer layer, the PCE of device was 12.5%. Thus, the combination of CuBuPc and GO could be a superior

alternative for the HTL due to the low-cost and simple preparation. Nouri *et al*.[154] developed stable normal PSCs using NiO_x-graphene oxide (NiO_x-GO) hybrids as hole-extraction materials. The photoluminescence and electrochemical impedance spectroscopy (EIS) measurements demonstrated that the introduction of GO into the NiO_x layer resulted in more efficient hole-extraction process from perovskite layer and more efficient suppressing of charge recombination at the perovskite/HTL interface. The conductivity of NiO_x layer was not improved due to the insulating property of GO. For the NiO_x-GO based device, a PCE of 13.3% was achieved with a V_{oc} of 1.03 V, a J_{sc} of 20.4 mA/cm^2 and an FF of 0.63. While the device with NiO_x as HTL obtained a PCE of 9.2% with a V_{oc} of 0.95 V, a J_{sc} of 19.0 mA/cm^2, and an FF of 0.51. To evaluate the long-term stability, the photovoltaic performances of devices were measured at different time intervals after keeping in a dry box of relative humidity of 28~32% under dark conditions. The devices with spiro-OMeTAD as HTL were reference devices. The spiro-based PSCs kept only 14% (Au electrode) of their initial PCE after 15 days of device operation. In contrast, NiO_x-GO based PSCs retained about 72% (carbon electrode) and 57% (Au electrode) of the original PCEs. The NiO_x-GO based devices exhibited much better stability which was attributed to the role of NiO_x-GO hybrids against the penetration of moisture.

In addition to the solution-processed graphene materials, the Hu *et al*. also reported the utilization of CVD-graphene film as a blocking layer between spiro-OMeTAD and Au top electrode in planar PSCs.[155] A single layer graphene was inserted into the spiro/Au interface through a simple lamination process. Although the efficiency slightly decreased after introduction of graphene layer, the air stability of the device was greatly improved. After aging for 96 h in air (humidity ~ 45%) or thermal annealing at 80 °C for 12 h, more than 94% efficiency of the devices with graphene can be maintained, which is much better than that of devices without graphene (~ 57%). The improved stability is attributed to the blocking effect of the graphene film, which can not only protect the perovskite film from the damage of moisture in air, but also block the undesirable migration of the metal iron into the perovskite layer. Therefore, CVD-

graphene films are promising as ultra-thin barrier against air and metal diffusion for the fabrication of high-performance PSCs with good long-term stability.

In summary, the employment of graphene and its derivatives in the PSCs with normal structure as HTLs, interlayers between perovskite and HTLs, or dopants for HTLs, can not only enhances the efficiency of PSCs, but also improve their ambient stability. The enhanced efficiency is due to the more efficient hole extraction and transfer after introduction of the graphene-based materials with high mobilities, while the improved device stability is mainly attributed to the hydrophobic nature of graphene-based materials, which prevents the infiltration of moisture from the air.

3.1.2 Inverted structure PSCs

In the PSCs with inverted structure, the HTLs play a vital role of extracting and transporting holes from perovskite to the electrode. In addition, the HTLs are of paramount importance to influence the quality of the growing perovskites. The morphology and crystallinity of perovskite are highly affected by the wettability of the HTL substrates. Thus, the HTLs with high conductivity and transparency, suitable wettability, and proper band energy structure are highly desirable. Recently, the graphene and its derivatives are investigated as HTLs or dopants for HTLs in inverted PSCs to enhance the photovoltaic performance and stability of PSCs.

Chen *et al*. developed oxo-functionalized graphene (oxo-G_1) as HTL for inverted PSCs to obtain a PCE of up to 15.2% and high ambient stability[156]. Due to the high work function of oxo-G_1, the V_{oc} could reach 1.1 V. Due to the excellent hydrophobicity of oxo-G_1, the environmental stability of the oxo-G_1-based PSCs were significantly enhanced. The unencapsulated devices could retain 80% of the initial PCE after 500 h illumination and keep 60% of the initial PCE after 1000 h of light soaking under 0.5 sun. In addition, 92% of the original PCE could be maintained after 1900 h stored in the ambient dark conditions. Lee *et al*.[157] employed GO/PEDOT:PSS composite as HTL to fabricate efficient and stable inverted PSCs. PSCs with composite HTL

exhibited a PCE of 9.7% which was higher than that of devices based on PEDOT:PSS showing a PCE of 8.2%. The higher photovoltaic performance was attributed to the decreased series resistance and increased shunt resistance. The introduction of GO improved the charge extraction and transport due to the better energy level alignment. Similarly, Niu *et al*.[158] used GO doped PEDOT:PSS as HTL to increase the PCE from 11.99% to 14.20%. The hole mobility of PEDOT:PSS was increased from 5.55×10^{-5} to 1.57×10^{-4} $cm^2V^{-1}s^{-1}$ by introducing GO as dopants. Yu *et al*. also investigated the effect of GO doped PEDOT:PSS on the performance enhance of inverted PSCs[159]. In addition to the aforementioned improvements, it was found that the crystallinity of perovskite prepared on the composite film was enhanced significantly. The presence of GO could facilitate the growth of perovskite along (110) orientation (Fig. 8a)[160]. The efficiency was boosted to 18.09%. Giuri *et al*. blended the graphene oxide and glucose with PEDOT:PSS to form nanocomposite as the HTL in the inverted perovskite solar cells [160] (Fig. 8b). The results suggested that the glucose molecule had a dual effect of reducing the GO and of improving the wettability of PEDOT:PSS substrate due to the presence of hydroxyl group terminations. The reduced GO increased the conductivity of PEDOT:PSS. The morphology of perovskite grown on the composite was significantly improved due to the suitable wettability of the substrate (Fig. 8c). The PCE of PSCs using composite as HTL was boosted to 12.8%. For the PEDOT:PSS as HTL, the PCE was 9.4% (Fig. 8d). It was noteworthy that the enhancement was mainly attributed to the higher V_{oc} reaching over 1.05 V. The high V_{oc} should be due to the present of a thin insulting caramelized glucose layer on top of PEDOT:PSS, which minimized the recombination losses at the HTL/perovskite interface.

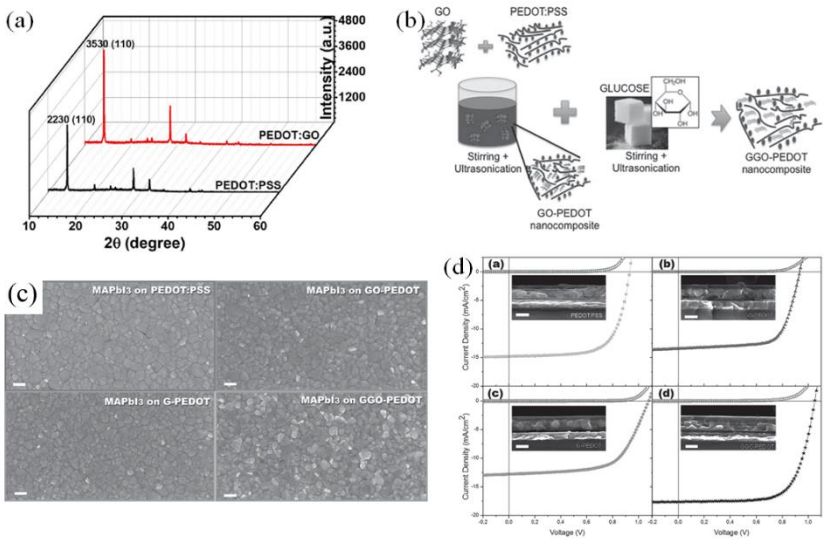

Fig. 8. (a) XRD patterns of perovskite films prepared on PEDOT:PSS and PEDOT:GO composite films with preferred orientation along the (110) directions. (b) A simplified sketch of the nanocomposite GO-PEDOT preparation. The hydrophilic edges of GO sheet and the glucose hydroxyl groups favor the dispersion in PEDOT:PSS polyelectrolyte. PEDOT:PSS has a necklace structure in which the hydrophilic PSS segments form blobs decorating the hydrophobic PEDOT chains, allowing a good and homogeneous interaction with hydrophilic GO sheets. (c) SEM morphology for perovskite films deposited on the different nanocomposite substrates. (d) *J-V* characteristics under AM 1.5G (100 mW cm^{-2}) simulated solar illumination (filled symbols) and in the dark (open symbols) for champion devices based on different substrates. Reproduced with permission from ref.[160].

Guo *et al*. proposed the combination of sulfated graphene oxide (sGO) and PEDOT:PSS as HTL to improve the photovoltaic performance of inverted PSCs [161]. The grain size of perovskite grown on the sGO-PEDOT:PSS composite was larger due to the higher contact angle of perovskite precursor droplets on the composite HTL than PEDOT. The larger grain size could lead to the decrease of defects in the films. The time-resolved photoluminescence spectra (TRPL) of perovskite films with PEDOT and sGO-PEDOT demonstrated that the composite layer had more efficient hole extraction due to the better energy level alignment. Based on the above enhances, the PCE was increased from 11.5% to 13.9 % by introduction of sGO into the PEDOT layer. Liu *et al*. introduced silver trifluoro-methanesulfonate (AgOTf) as dopant in GO films to simultaneously decrease the work function and sheet resistance [162]. The inverted PSCs based on PEDOT:PSS:AgOTf-doped GO demonstrated a PCE of 11.90% higher than a PCE of 10.70% from the devices using PEDOT:PSS as HTL. Wang *et al*. proposed to

dope PEDOT:PSS with the UV-Ozone treated rGO to improve the morphology and hole mobility of HTLs[163]. The UV-Ozone treated rGO can be homogeneously dispersed in deionized water and the formed film owned low roughness. The PSCs based on rGO/PEDOT:PSS as HTL demonstrated better photovoltaic performance with a maximum PCE of 10.75%. The devices using pristine PEDOT:PSS as HTL obtained a maximum PCE of 8.48%. Cho *et al*. modified the surface chemistry and morphology of graphene oxide by γ-ray irradiation [164]. The GO was further oxidized and could be more easily dispersed in water. The introduction of γ-GO into the PEDOT:PSS hole transport layer improved the hole mobility and charge collection. Moreover, the γ-GO embedded PEDOT:PSS HTL demonstrated more hydrophobic which assisted the growth of perovskite films with large grains. The resulted PCE of devices exhibited a maximum PCE of 12.76%, higher than the PEDOT:PSS based devices showing a maximum PCE of 10.61%. Jokar *et al*. investigated the efficiency of hole extraction and transport based on GO and rGO with different reduction extent as HTLs in inverted perovskite solar cells [165]. The photoluminescence and transient photoelectric decays suggested that the oxygen group in GO was beneficial for the hole extraction from perovskite to GO layers. While the oxygen group in GO could also lead to the intense charge recombination. The reduction of the oxygen-containing groups in GO could significantly reduce the ability of hole extraction from perovskite to rGO and retard the charge recombination rate. The devices based on 4-hydrazinobenzenesulfonic acid (HBS) reduced GO (rGO-HBS) and hydrazine reduced GO (rGO-NH) as HTLs obtained PCEs of 16.4% and 16.0%, respectively. For GO based PSCs, the maximum PCE was 13.8%. Yang *et al*. optimized the thickness of GO film as HTLs to simultaneously obtain the GO layer with high work function and conductivity. The PSCs based on optimized GO layer achieved a maximum PCE of 16.5% [166]. The encapsulated devices retained more than 80% of their initial efficiency for 2000 h testing under high humidity and continuous light soaking. Bhosale *et al*. used MoO_x nanoparticles functionalized GO films as HTLs for inverted PSCs.[167] The functionalization of GO films with MoO_x increased the work function of GO film and retarded the charge recombination in the perovskite/GO interface, which results in

enhanced V_{oc} and J_{sc} of the device, attaining a PCE of 16.7%. Nouri *et al*. used GO as HTL and lithium-functionalized graphene oxide as ETL to fabricate inverted PSCs [168]. The well-matched band energy level enabled to obtain a maximum PCE of 10.2% with Ti-sol as in interfacial layer between perovskite and Li-GO.

Sun *et al*. introduced GO sheets into the ITO/perovskite interface as the nucleation sites assisting the crystal growth of perovskite to enhance the performance of HTL-free PSCs [169]. The grain size of perovskite films grown on GO sheets was about twice of that on bare ITO substrate. The efficiency was boosted from 4.78% to 6.62% by the employment of GO sheets. Kim *et al*. proposed nitrogen-doped graphene oxide nanoribbons (NGONR) as a hole transport layer in inverted PSCs [170]. The highest occupied molecular orbital (HOMO) and the lowest unoccupied molecular orbital (LUMO) levels of NGONR were 5.64 eV and 3.43 eV, respectively. These values were well-matched with the valence (VB) and conduction bands (CB) of the $CH_3NH_3PbI_3$ layer (VB: 5.3 eV and CB: 3.8 eV), respectively. The efficient hole extraction and transport enhanced performance of PSCs with a maximum PCE of 12.94 %.

Li *et al*. employed GO/PEDOT:PSS multilayer as HTL for inverted PSCs [171] (Fig. 9a). This strategy takes advantages of high conductivity of PEDOT:PSS and electron blocking ability of GO. Due to the energy level match, holes could be efficiently extracted and collected from perovskite to ITO electrode (Fig. 9b). Besides, electrons could be significantly blocked due to the higher LUMO of GO than that of perovskite. Thus, the introduction of GO could reduce leakage current and charge recombination. The efficiency was increased from 10.0% to 13.1% by incorporation of GO. Zhou *et al*. employed a rGO/ploytriarylamine (PTAA) bilayer as HTL to fabricate inverted PSCs with high efficiency and stability [172] (Fig. 9c). Due to the cascading energy level alignment, the capacity of hole extraction and transport was enhanced significantly (Fig. 9d). Moreover, the rGO layer owns strong absorptance in the near-UV region (300-400 nm). Thus, this cut-off of UV light improved the light-soaking stability of PSCs. Based

on these advantages, the PSCs based on a rGO/ PTAA bilayer achieved a maximum PCE of 17.2% with an area of 1.02 cm^2. In addition, the PSC retained about 90% of its initial efficiency after continuous one sun illumination of 500 h.

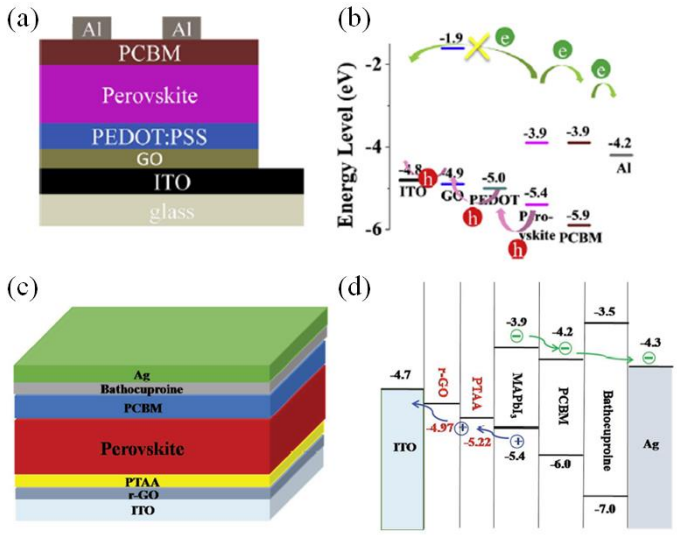

Fig. 9. (a) Device architecture and (b) the corresponding energy-band diagram of the devices with GO and PEDOT:PSS hybrid bilayer as the HTL. Reproduced with permission from ref.[171]. (c) Diagram of the device architecture. (d) Energy-level diagram for the device. Reproduced with permission from ref.[172].

Luo *et al*. spin-coated a GO layer onto the PEDOT:PSS HTL to enhance the efficiency and stability of PSCs [173]. The GO modified PEDOT:PSS exhibited superior wettability and enabled the growth of full-coverage and pin-hole free perovskite film. The GO layer suppressed the charge recombination significantly. The PSCs with incorporation of GO achieved a maximum PCE of 15.34%, higher than a maximum PCE of 11.90% for the refence devices. Feng *et al*. proposed the use of PEDOT:PSS-ammonia modified graphene oxide (GO: NH_3) bilayer HTL to enhance the performance of PSCs [174]. The introduction of GO:NH_3 layer formed a better energy alignment between ITO and the perovskite layer. The capacity of charge extraction and transport was improved. Moreover, the perovskite deposited on the GO:NH_3 demonstrated higher crystallinity and more preferred orientation, which was in favor of charge transport. The maximum efficiency was increased from 12.50% to 16.11%. Wang *et al*. used GO and MoS_2 as interfacial layers to modify the work functions of PEDOT:PSS and Ag to obtain better energy level matches which could suppress the charge non-recombination and enhance

the charge extraction [175]. With the incorporation of GO and MoS_2, the V_{oc} was increased from 0.962 V to 1.135 V and the maximum PCE was boosted from 14.15% to 19.14%.

In summary, graphene and its derivatives exhibit plenty of merits as HTLs in inverted PSCs. The suitable wettability enables the growth of perovskite film with high quality. The high work function enables the ohmic contact between graphene related HTL and ITO electrode, which decrease the series resistance of the device. The 2D structure prevents the water and oxygen efficiently, which enhances the ambient stability of the devices.

3.2 Transition metal dichalcogenides and other 2D materials

Transition metal dichalcogenides (TMDs), such as MoS_2 and WS_2, are also promising superior HTL candidates due to their high carrier mobility, tunable bandgap and versatile processing methods [176-178]. Recently, many groups make efforts to fabricate PSCs with high efficiency and stability by employing different 2D materials as HTLs.

3.2.1 Normal structure PSCs

Capasso *et al*. employed liquid-phase exfoliated MoS_2 as a buffer layer between perovskite and spiro-OMeTAD layers [179] (Fig. 10a-b). The MoS_2 buffer layer played two roles: preventing the formation of shunt paths between perovskite and the back electrode; facilitating the hole extraction from perovskite to spiro-OMeTAD. The PSCs with MoS_2 buffer layer achieved a maximum PCE of 13.3% (Fig. 10c-d). Besides, the PCE of PSCs with MoS_2 retained about 93% of its initial value after about 550 h illumination. For the reference devices without MoS_2, the PCE was degraded to 66% of the initial value. Muduli *et al*. [180] used BP nanosheets processed with liquid exfoliation method as buffer layer between perovskite and spiro-OMeTAD layers. Due to the well-matched energy level alignment, the PCE of devices with BP reached 16.4 %.

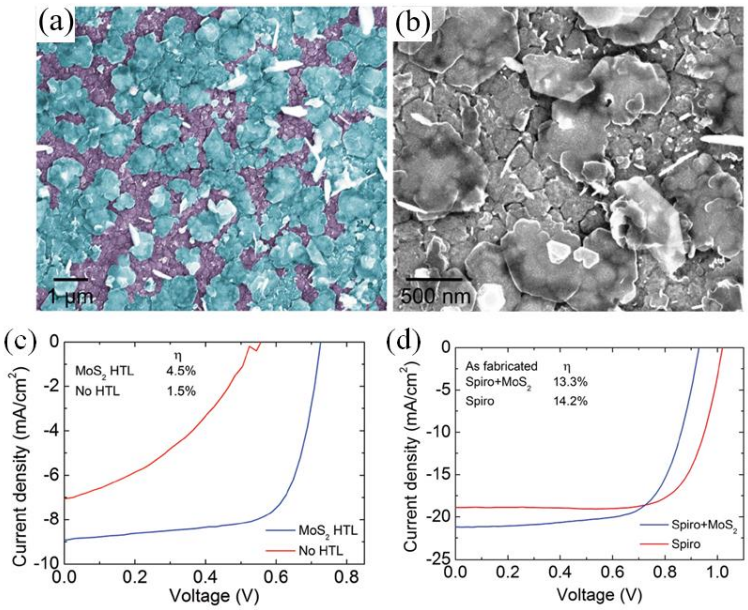

Fig. 10. SEM images of the MoS_2 flakes spin-coated onto the perovskite layer of the cell. (a) Image in false colors (dark cyan for MoS_2 flakes and purple for the underlying perovskite layer) highlighting the coverage provided by the spin-coating process of the MoS_2 flakes. (b) MoS_2 flakes on top of the perovskite crystals. (c) *J-V* curves of the cells fabricated with MoS_2 HTL and without HTL (0.1 cm^2 active area). (d) *J-V* curves of the cells measured after fabrication (0.1 cm^2 active area). Reproduced with permission from ref.[179].

3.2.2 Inverted structure PSCs

Kim *et al*. proposed MoS_2 and WS_2, which were prepared by chemical vapor deposition method, as HTL to fabrication inverted PSCs [181] (Fig. 11a). Due to the proper energy band matching (Fig. 11b), the devices based on MoS_2 and WS_2 obtained 9.53% and 8.02%, respectively. Kakavelakis *et al*. used liquid-phase exfoliation processed MoS_2 flakes as interlayer between PTAA and perovskite layers to obtain inverted PSCs with high efficiency and stability [182] (Fig. 11c). The insertion of MoS_2 enhanced the hole extraction ability (Fig. 11d). The maximum PCE was increased from 15.51% to 16.42% with the incorporation of MoS_2. Moreover, the presence of MoS_2 could block the contact between PTAA and perovskite. The dopant materials (F4-TCNQ) in PTAA intent to introduce moisture into the PTAA/perovskite interface, which accelerated the degradation of perovskite. Owing to the presence of MoS_2, the encapsulated MoS_2 modified devices could keep 80% of initial PCE after 568 h of continuous illumination at maximum power output in ambient conditions. Dai *et al*. developed a composite HTL prepared by blending phenyl acetylene silver (PAS)-functionalized MoS_2 with PEDOT:

PSS [183]. The PSCs based on the composite HTL achieved a maximum PCE of 16.47%. The reference devices without MoS_2 obtained a maximum PCE of 14.69%. The performance enhancement is attributed to the improved hole extraction and transfer ability. Dasgupta *et al*. prepared MoS_2 HTL by centrifugal casting method to fabricate inverted PSCs [184]. The developed MoS_2 film owned superior coverage and excellent morphology. The PSCs based on this MoS_2 HTL achieved a maximum of 6.01%. Huang *et al.* proposed to use water-soluble MoS_2 and WS_2, processed by exfoliating the bulk materials with lithium intercalation reaction, as HTLs to fabricate inverted PSCs [185]. They found that 1T-rich TMDs prepared without annealing demonstrated higher performance than 1T-poor TMDs with post-annealing. The best efficiency of PSCs based on MoS_2 and WS_2 reached 14.35% and 15.0%, respectively. Due to the inorganic HTLs, the stability of PSCs with TMDs were significantly enhanced.

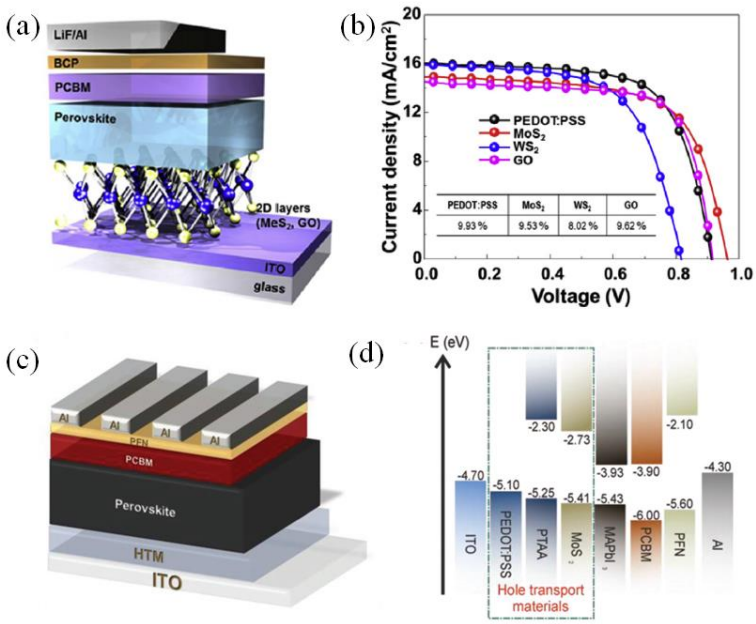

Fig. 11. (a) Schematic illustration of PSC fabrication procedure and device structure. (b) *J-V* curves of each different HTL-based PSCs. The maximum efficiency of PEDOT:PSS, MoS_2, WS_2, and GO layers are 9.93%, 9.53%, 8.02%, and 9.62%, respectively. Reproduced with permission from ref.[181]. (c) Schematic diagram of device structure. (d) Energy-band diagram under flat-band condition of the fabricated planar inverted PSCs. Reproduced with permission from ref.[182].

Chen *et al.* employed BP quantum dots (BPQDs) as an interlayer between PEDOT:PSS and perovskite to enhance the hole extraction ability [186] (Fig. 12a). In addition to the

enhanced hole extraction rate (Fig. 12b), the grain size of perovskite film deposited on the BPQDs was increased. By optimizing the thickness of BPQDs layer, the PSCs with BPQDs achieved a maximum PCE of 16.69%. The PCE of reference devices with BPQDs obtained a maximum PCE of 14.10% (Fig. 12c).

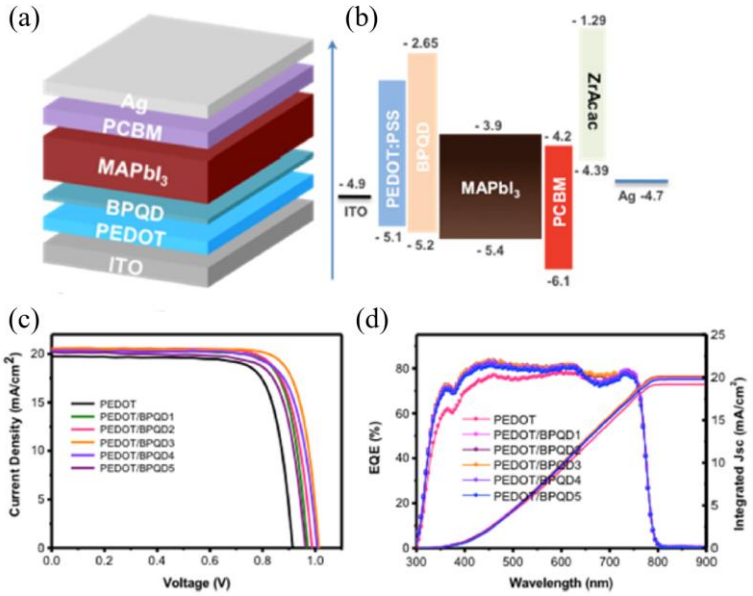

Fig. 12. (a) Device configuration of the p-i-n planar PSCs. (b) Energy level diagram of each layer in the device. (c,d) *J-V* and EQE curves of the PSCs with BPQDs of different thickness. Reproduced with permission from ref.[186].

In summary, TMDs have shown great potential as HTLs due to their excellent optoelectronic properties, such as high carrier mobility, tunable bandgap and dangling-bond free surface. However, the efficiencies of PSCs based TMD HTLs are still much lower so far. The main limitation is the lack of method to prepare 2D materials films with superior morphology, which should be the focus of the future research on high performance PSCs with 2D materials as CTLs.

Table 2. Summary of the PSCs with HTLs based on 2D materials.

Normal or Inverted structure	Categories of 2D materials	Planar or Mesoporous	Device structures	PCE (%)	Ref.
Normal	graphene	Mesoporous	glass/FTO/TiO_2/$MAPbI_3$/TSHBC+Graphene/Au	14.02	[187]
Normal	graphene	Planar	glass/FTO/TiO_2/$MAPbI_3$/P3HT+F-Graphene/Ag	13.82	[146]
Normal	graphene	Mesoporous	glass/FTO/c-TiO_2/mp-TiO_2/$MAPbI_3$/PEDOT+Graphene/Au	8.79	[145]
Normal	graphene	Planar	Glass/FTO/TiO_2/$MAPbI_3$/amino-graphene/spiro-OMeTAD/Au	14.60	[147]

Normal	rGO	Mesoporous	glass/FTO/c-TiO_2/mp-TiO_2/$MAPbI_3$/rGO/spiro-OMeTAD/Ag	10.60	[148]
Normal	rGO	Planar	glass/ITO/ZnO/C60/$MAPbI_3$/PEDOT+Fluorinated-rGO/MoO_3/Ag	14.90	[149]
Normal	rGO	Planar	glass/ITO/TiO_2/rGO+mp-TiO_2/$MAPbI_3Cl_{3-x}$/rGO-4FPH/spiro-OMeTAD/Au	18.75	[150]
Normal	rGO	Planar	glass/FTO/TiO_2/$MAPbI_3$/B-rGO paper/FTO	8.96	[151]
Normal	GO	Mesoporous	glass/FTO/c-TiO_2/mp-TiO_2/$MAPbI_3$/GO/spiro-OMeTAD/Au	15.10	[152]
Normal	GO	Mesoporous	glass/FTO/c-TiO_2/mp-TiO_2/rGO/$MAPbI_3$/GO/CuBuPc/Au	14.40	[153]
Normal	GO	Mesoporous	glass/FTO/c-TiO_2/mp-TiO_2/$MAPbI_3$/NiO_x+GO/Au	13.30	[154]
Normal	CVD graphene	Planar	glass/FTO/TiO_2/$MAPbI_3$/spiro-OMeTAD/graphene/Au	15.7%	[155]
Inverted	GO	Planar	glass/ITO/PEDOT:PSS+GO/$MAPbI_3$/PCBM/ZnO/Ag	18.09	[159]
Inverted	GO	Planar	glass/ITO/PEDOT:PSS+GO+Glucose/$MAPbI_3$/PCBM /Al	12.80	[160]
Inverted	Sulfated GO (s-GO)	Planar	glass/ITO/PEDOT:PSS+s-GO/$MAPbI_3$/PCBM/Ag	13.90	[161]
Inverted	GO	Planar	glass/ITO/PEDOT:PSS+AgOTf-doped GO/$MAPbI_3$/PCBM/Ag	11.90	[162]
Inverted	γ-ray GO	Planar	glass/ITO/PEDOT:PSS+γGO/$MAPbI_3$/PCBM/Al	12.76	[164]
Inverted	MoOx nanoparticles modified GO	Planar	glass/ITO/GO+MoOx/$MAPbI_3$/PCBM/Ag	16.7%	[167]
Inverted	Nitrogen-doped GO (NGONR)	Planar	glass/ITO/NGGO/$MAPbI_3$/ZnO/Al	12.94	[170]
Inverted	Ammonia modified GO (GO:NH_3)	Planar	glass/ITO/PEDOT:PSS/GO:NH_3/GO/$MAPbI_3$/PCBM/Ag	16.11	[174]
Inverted	Oxo-functionalized graphene (oxo-G_1)	Planar	glass/ITO/PEDOT:PSS/oxo-G_1/$MAPbI_3$/PCBM/ZnO/Al	15.2	[156]
Inverted	rGO	Planar	glass/ITO/r-GO/PTAA/ $MAPbI_3$/PCBM/Bathocuproine/Ag	17.2	[172]
Normal	MoS_2	Mesoporous	glass/FTO/c-TiO_2/mp-TiO_2/$MAPbI_3$/MoS_2/spiro-OMeTAD/Au	13.3	[179]
Normal	BP	Mesoporous	glass/FTO/c-TiO_2/mp-TiO_2/$MAPbI_3$/BP/spiro-OMeTAD/Au	16.4	[180]
Inverted	MoS_2	Planar	glass/ITO/MoS_2/$MAPbI_3$/PCBM/Li/Al	9.53	[181]
Inverted	MoS_2	Planar	glass/ITO/PTAA/MoS_2/$MAPbI_3$/PCBM/PFN/Al	16.42	[182]
Inverted	Phenyl acetylene silver (PAS)-MoS_2	Planar	glass/ITO/PEDOT:PSS+PAS-MoS_2/$MAPbI_3$/PCBM/Ag	16.47	[183]
Inverted	WS_2	Planar	glass/ITO/WS_2/$MAPbI_3$/C_{60}/BCP/Ag	15.00	[185]
Inverted	BPQDs	Planar	glass/ITO/PEDOT:PSS/BPQDs/$MAPbI_3$/PCBM/Ag	16.69	[186]

Note: c-TiO_2 indicate the compact layers of TiO_2, while mp-TiO_2 means mesoporous layers of TiO_2. GO and rGO stand for graphene oxide and reduced graphene oxide, respectively.

4. 2D materials for electron transporting

The ideal electron transport layers (ETLs) in PSCs should have high electron mobilities, efficient hole blocking ability, good chemical stability, and proper LUMO levels that can match well with the perovskite LUMO level. Therefore, a variety of 2D materials, especially graphene and its derivatives, are of great advantages being used as ETLs in PSCs, as discussed in this part bellow. Compared with the mostly often used electron

transporting materials in PSCs, including n-type metal oxides (TiO_2, SnO_2, ZnO, etc.), fullerene-based materials (C_{60}, PCBM, etc.) and some n-type conjugated polymers, graphene and its derivatives not only have high mobilities and good stability but also have tunable energy levels (by chemical doping), which can meet different device designs. Generally, they can be adopted as ETLs independently, or combined with other organic or inorganic electron transporting materials for electron transporting. And they can also be used as interfacial buffer layers at the perovskite/ETL or ETL/electrode interfaces, to improve the electron transport or the device stability. In many cases, the graphene-based ETLs often show better electron transporting properties and contribute to the higher PCEs and superior long-term stabilities of the devices. In this part, recent work about using 2D materials for electron transporting will be reviewed systematically, as listed in Table 3.

4.1 Graphene and its derivatives for electron transporting

4.1.1 Normal structure PSCs

Graphene

In 2013, Henry Snaith and coworkers[188] firstly reported the introduction of pristine graphene flakes for electron transporting in PSCs. The few-layer graphene flakes (100 nm ~ 1μm in dimensions, and ~ 3.1 nm in thickness) were exfoliated and dispersed in isopropanol by using a liquid-phase exfoliation method (under ultrasonication for ~ 70 hours) with graphite flakes as raw material. Nanocomposites of pristine graphene flakes and anatase-TiO_2 nanoparticles (prepared by a hydrothermal method) were employed as the ETL in normal-structured PSCs with a device structure of glass/FTO/TiO_2+graphene/Al_2O_3/perovskite/spiro-OMeTAD/Au, as shown in Fig. 13a-b. Note that the graphene/TiO2 film was prepared by low temperature solution process (<150ºC) without high-temperature sintering. It can be noticed from Fig. 13c that the introduction of graphene flakes in TiO_2 layer showed a remarkable enhancement of the device performance. The low-temperature processed PSCs with graphene/TiO_2 as ETLs achieved a champion efficiency of 15.6% (as shown in Fig. 13d), which was even higher than the devices with high-temperature sintered TiO_2 films. The optimized

concentration of graphene in TiO_2/graphene nanocomposites was 0.6 wt.%, which just corresponded to the monolayer coverage of TiO_2 nanoparticles on graphene surface. The improved photovoltaic performance was mainly ascribed to two reasons. First, the work function of graphene (-4.4 eV) matches well with the energy level of FTO and TiO_2 (as indicated in Fig. 13b), which reduces the formation of energy barriers at the FTO/TiO_2 interface and therefore lead to better electron extraction property. Second, the superior charge mobility of the pristine graphene material increased the conductivity of the TiO_2 layer, and reduced the series resistance of the device, which was confirmed by the series resistance values extracted from both *J-V* curves and impedance spectra of the PSCs. This work demonstrated that the nanocomposites of graphene and TiO_2 have great potential when used as ETLs for highly efficient low-temperature processed PSCs. There are also reports of PCE enhancements through the incorporation of graphene in compact or mesoporous TiO_2 layers, although the graphene/c-TiO_2 or graphene/mp-TiO_2 films still need sintering at high temperatures (~450 ºC).[189-191] Agresti *et al*.[190] prepared efficient solar modules with over 12.5% PCEs and active area up to 50 cm^2. They doped mp-TiO_2 layer with graphene and employed lithium-neutralized graphene oxide as interlayer at the interface between perovskite and mp-TiO_2 layers, indicating a potential method for large-area fabrication of high-efficient perovskite solar panels.

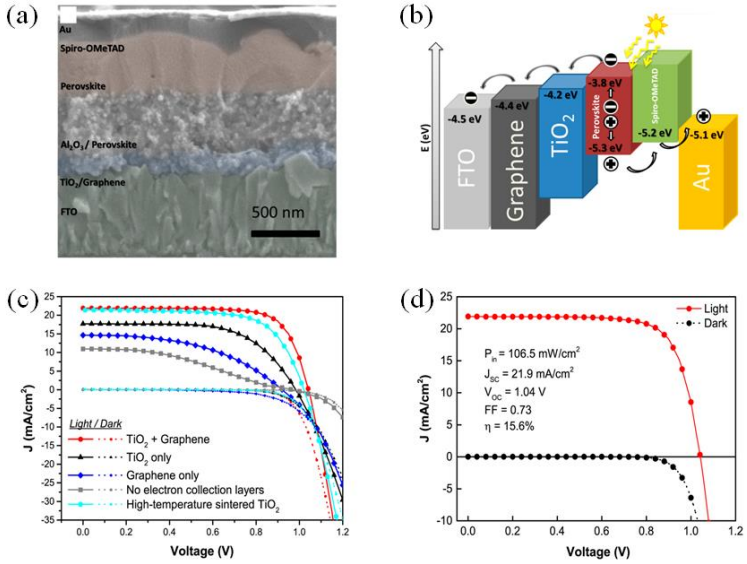

Fig. 13. (a) The cross-sectional SEM image demonstrating the device structure of glass/FTO/TiO_2+graphene/Al_2O_3/perovskite/spiro-OMeTAD/Au. (b) The schematic energy level

diagram of the device. (c) *J-V* curves of PSCs with different ETLs. (d) *J-V* curves of the champion device with nanocomposite of TiO_2 and graphene as ETL. Reproduced with permission from ref.[188].

Beyond combination with TiO_2, graphene has also been integrated with other metal oxides, such as SnO_2[192], ZnO[193] and $SrTiO_3$[194], working as excellent ETLs for efficient normal-structured PSCs. Zhao *et al.*[192] achieved a high efficiency of 20.2% and an remarkably improved FF of 82% in planar PSCs by doping the SnO_2 layer with graphene, which was modified with a N,N'-bis-[2-(ethanoic acid sodium)]-1,4,5,8-naphthalene diimide (NDI) surfactant. The SnO_2/graphene ETL was prepared by spin-coating from $SnCl_2{\cdot}2H_2O$ solution in ethanol with addition of NDI-modified graphene. Fig. 14a shows the device structure and the schematic diagram of the $N{-}H\cdots I^-$ van der Waals interaction between the hydrogen atoms of the NDI and the iodine of perovskite crystals, which was confirmed by nuclear magnetic resonance spectroscopy (NMR) measurements (as shown in Fig. 14b) and electron localization function (ELF) calculations. This interaction can fix the octahedral $[PbI_6]^{4-}$ at the perovskite/SnO_2 interface. Besides, the incorporation of graphene also tuned the band alignment for electron transport and increased the electrical conductivity as well as the electron mobility of the SnO_2 films, which was ascribed to the high conductivity and mobility of graphene. Therefore, the NDI-graphene/SnO_2 nanocomposites offered more efficient extraction and transport of the photoinduced electrons, contributing to the high efficiencies.

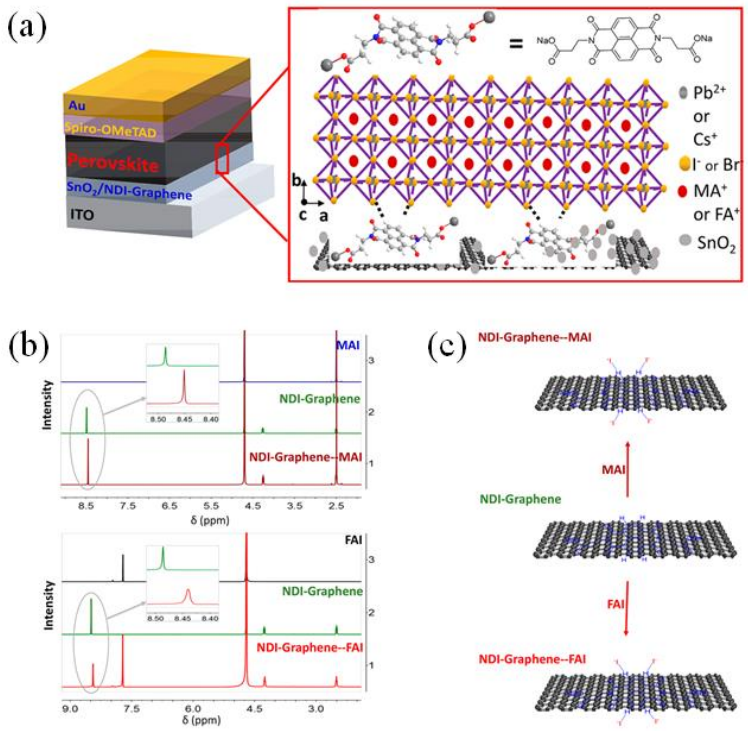

Fig. 14. (a) Schematic architecture of the PSC with graphene incorporated SnO_2 as ETL. The expanded diagram shows the structure of the NDI and the bonding condition between perovskite and NDI-graphene films at the interface. (b) The ^{1}H NMR spectra of MAI, FAI, NDI-Graphene, NDI-Graphene-MAI and NDI-Graphene-FAI. (c) The schematic diagram showing the van der Waals interaction between NDI-graphene and MAI and FAI. Reproduced with permission from ref.[192].

Graphene quantum dot

Graphene quantum dots (GQDs), as the zero-dimensional (0D) form of graphene materials, have also been used for electron transporting in normal-structured PSCs. The 0D GQDs have tunable bandgaps because of the quantum-confinement and edge effects, which make them distinct from the 2D graphene fakes.[195] The small size of GQDs (normally smaller than 10 nm) make it much easier to be coated uniformly at interfaces or dispersed evenly in other n-type materials. The GQDs-modified ETLs (such as TiO_2[196-198], SnO_2[199] and PCBM[200]) show superior electronic properties for applications in PSCs. Zhu *et al.*[196] first utilized ultrathin GQDs at the perovskite/ETL interface to facilitate electron transfer from the perovskite layer to the ETLs and cathodes. The device consisted a structure of glass/FTO/c-TiO_2/mp-TiO_2/GQDs/$MAPbI_3$/spiro-OMeTAD/Au, as shown in Fig. 15a. The GQDs were synthesized through a facile electrochemical method.[201] The aqueous solution of

GQDs (with average size between 5 nm and 10 nm) was uniformly coated on the surface of mp-TiO_2 films. The device performance was greatly improved after inserting of this GQD layer, as shown in Fig. 15b, which was mainly attributed to the increased photocurrent. The origin of this enhancement was confirmed (by femtosecond transient absorption measurements) to be the much faster electron extraction speed from perovskite to TiO_2 with the presence of GQDs than without GQDs. This work highlighted that GQDs can work as a superfast electron tunnel for efficient mesoporous PSCs. Besides, Ryu *et al.*[197] also employed GQDs to modify the compact TiO_2 layer for efficient planar PSCs (as shown in Fig. 15c). The effects of GQD size on the device performance was investigated. Fig. 15d shows the corresponding *J-V* curves, indicating the notable improvement in all the photovoltaic parameters of the PSCs with GQD modification. In addition to the accelerated electron extraction, it was illustrated that the GQD layer with appropriate size could effectively improve the perovskite crystallinity, lower the series resistance of the perovskite/TiO_2 interface, and reduce the *J-V* hysteresis. As a result, a best PCE of 19.11% was achieved.

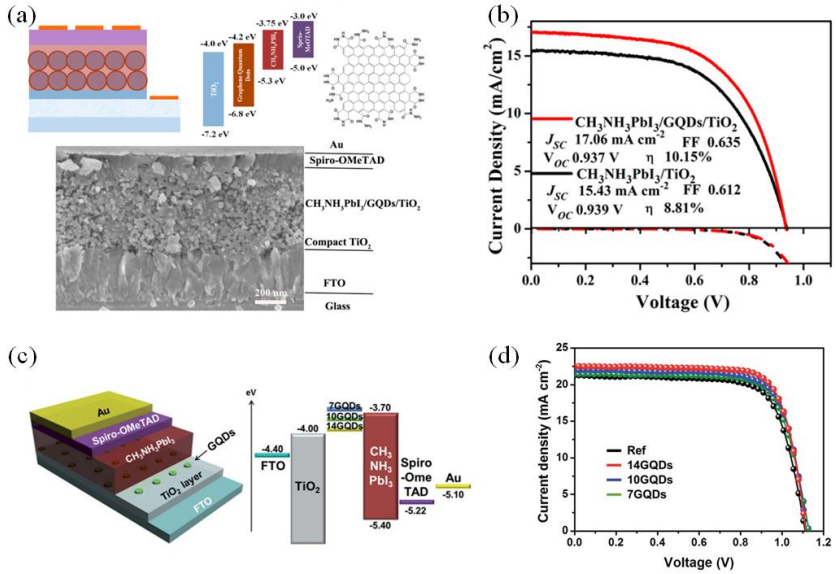

Fig. 15. (a) Schematic diagrams of the device structure, energy levels, the GQDs with modified edges, and the cross-sectional SEM image of the device. (b) *J-V* curves for the PSCs with and without GQDs coating on top of the mp-TiO_2 films. Reproduced with permission from ref.[196]. (c) Schematic diagrams of the planar PSC with GQDs-modified compact TiO_2 layer. (d) *J-V* curves showing the size effects of the GQDs on the device performance. Reproduced with permission from ref.[197].

Recently, the planar PSCs based on GQDs incorporated SnO_2, reported by Xie *et al*.[199], have demonstrated a high steady-state efficiency of 20.23%, as shown in Fig. 16. The TEM image in Fig. 16a indicated that the GQDs was highly crystallized with average size of 5-10 nm. A small amount of GQDs (optimum value ~ 1 wt.%) were added into the $SnCl_2 \cdot 2H_2O$ ethanol solution, which was spin-coated on ITO substrates to form a thin and uniform SnO_2:GQDs layer (~ 40 nm), as can be clearly observed in Fig. 16d. The conductivities of the bare SnO_2 and SnO_2:GQDs films were studied by characterizing the *J-V* curves of the ITO/SnO_2:GQDs/Ag device (see Fig. 16b) under a bias voltage of 0.1 V. The conductivity of the SnO_2:GQDs film was a little bit higher than the bare SnO_2 film in the dark. However, under light illumination, as shown in Fig. 16b, the conductivity of the SnO_2:GQDs film increased dramatically for about 20 times, while the conductivity of bare SnO_2 film only show slight improvement. This phenomenon can be explained with the schematic diagram in Fig. 16c. Under light illumination, GQDs will absorb photons (with energy higher than the bandgap of GQDs, 2.4eV) and generate a large number of free electrons and holes, of which the electrons will be injected into the SnO_2 quickly before recombination due to the matching energy levels and the long carrier lifetime[202] in GQDs. These injected electrons will first fill the electron traps (mainly attributed to the oxygen vacancies) of SnO_2 and then accumulate in the SnO_2 film, which will dramatically increase the electron concentration in the SnO_2 film. Besides, the space charge limited current (SCLC) measurements also demonstrated that the electron trap-state density of SnO_2:GQDs film decreased from 4.3×10^{16} to 1.23×10^{16} cm^{-3} upon light illumination, while its electron mobility increased from 6.72×10^{-4} to 1.01×10^{-3} $cm^2V^{-1}s^{-1}$. Therefore, the greatly increased conductivity and mobility of the SnO_2 film after incorporating of GQDs, significantly improved electron extraction efficiency of the ETL and reduced the charge recombination in the device, which contributed the high-efficiency PSCs with reduced *J-V* hysteresis and improved stability, as shown in Fig. 16f-i.

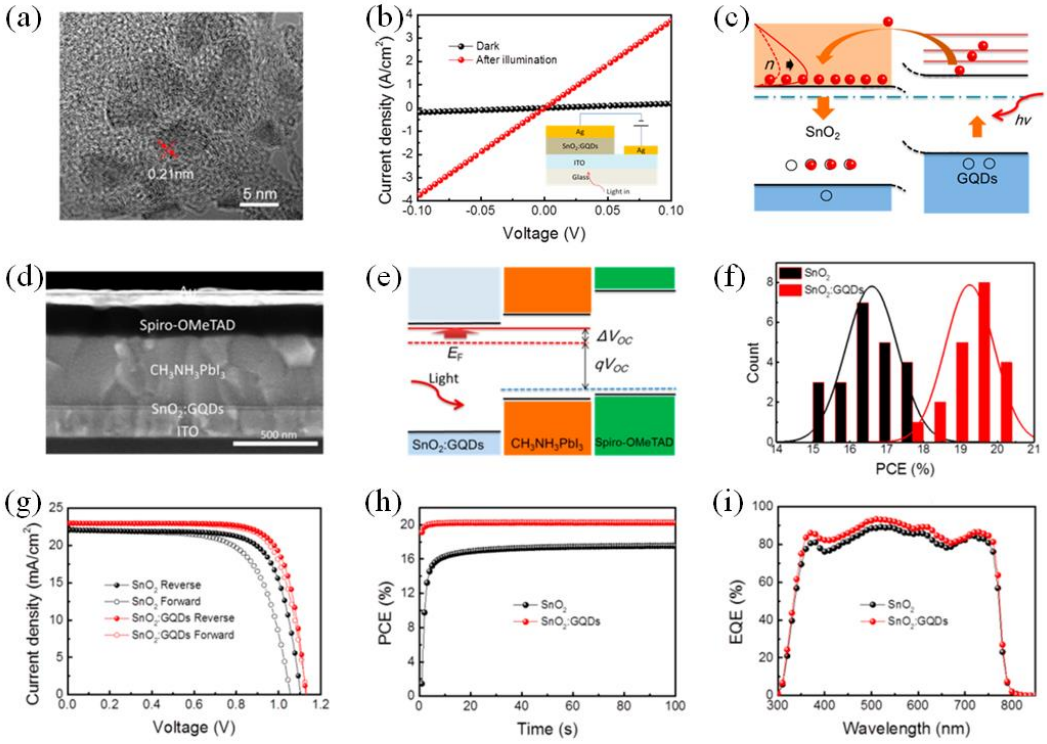

Fig. 16. (a) TEM image of the GQDs. (b) *J-V* characteristics showing the conductivity change of SnO_2:GQDs film under illumination. (c) Schematic diagram of the hot electron transfer from GQDs to SnO_2 under illumination. (d) Cross-sectional SEM image of the PSC with a structure of glass/ITO/SnO_2+GQDs/$MAPbI_3$/spiro-OMeTAD/Au. (e) The corresponding energy level diagram of the device. (f-i) Histogram of the PCE values, *J-V* characteristics, stabilized PCEs, and EQE spectra of the PSCs based on bare SnO_2 and SnO_2:GQDs. Reproduced with permission from ref.[199].

Reduced graphene oxide

Normally, reduced graphene oxide (rGO) can be obtained through the chemical oxidation and exfoliation of graphite, followed by chemical reduction of GO, which makes rGO regain the high electronic conductivity. Although the synthesized rGO flakes will inevitably contain some lattice defects, it offers a high-yield production method for graphene sheets. And similar with graphene, the rGO nanoflakes can also be used for electron transporting. They have been successfully used for integration with TiO_2[153, 203-205], ZnO[206], $ZnSnO_4$[207] and even polymers[208], or for interfacial modifications[209, 210]. Han *et al.*[203] demonstrated a performance enhancement of mesoporous PSCs by introducing rGO in the mp-TiO_2 layers. Compared with pure mp-TiO_2 films, the rGO/mp-TiO_2 nanocomposite films reduced the interfacial resistance and thus improved the charge collection efficiency. Effects of rGO contents in the mp-

TiO_2 layer were studied. The champion device of 14.5% efficiency was achieved with an optimal rGO content of 0.4 wt.%. Later, Cho *et al*.[205] also achieved a much higher efficiency (19.54%) by mixing rGO flakes with mp-TiO_2 and subsequent Li-TFSI treatment ($(FAPbI_3)_{0.85}(MAPbBr_3)_{0.15}$ perovskite was employed). PSCs fabricated with rGO incorporation in different layers (including the mp-TiO_2, perovskite and spiro-OMeTAD layers) were compared. The result was that the addition of rGO had a beneficial effect on the device performance only when rGO was mixed with the mp-TiO_2 layer. Shunt pathways were formed when rGO was added in perovskite or HTLs, which negatively affected the device performances. In addition to the mp-TiO_2 scaffold, rGO can also be integrated into the mesoporous scaffolds of Zn_2SnO_4 nanofibers[207] or polyaniline[208]. Tavakoli *et al*.[210] even prepared a three-dimensional scaffold of rGO with a ultra-large surface area by using an electrophoretic process, and yielded a 27% PCE improvement when the rGO scaffold was used a interlayer between c-TiO_2 and perovskite films. These successful applications indicate that rGO and its composites are promising alternative electron transporting materials for PSCs.

4.1.2 Inverted structure PSCs

Graphene

Recently, graphene and functionalized graphene have also been used for electron transporting in PSCs with inverted structure.[211-213] Castro *et al*.[211] reported the synthesis of cove-edge graphene nanoribbons (GNs) and their applications as novel ETLs in inverted PSCs. It turned out that the GNs-based ETLs outperformed PCBM in efficiencies due to the better energy level alignment and more efficient electron transport, exhibiting maximum PCEs of 15.6% and 16.5% for the two GNs, while the highest efficiency that the PCBM-based PSCs could get was 14.9%. Additionally, these two GNs are more hydrophobic than PCBM, which therefore contributed to the improved long-term stability of the devices. Later, based on the graphene nanoribbons, they further synthesized three-dimensional (3D) graphene nanostructures[212] through coupling and fusion of a central triptycene hub and helical graphene nanoribbons. The PSCs employing the 3D graphene nanostructures as ETLs yielded a high PCE of 18.0%

as a result of the 3D architecture and the reduced interfacial resistance. Kim *et al.*[213] reported the utilization of edged-selectively graphene fluorine functionalized graphene nanoplatelets (EFGnPs-F) at the interface between PCBM and top electrodes in inverted-structure PSCs, as shown in Fig. 17. Although the EFGnPs-F-based PSCs achieved quite similar PCEs with the control devices (without EFGnPs-F interlayers), the device stability was dramatically improved with the presence of the EFGnPs-F interlayers. With the modification of EFGnPs-F at the PCBM/Al interface, the PSCs maintained ~ 82% of the initial efficiencies after exposure in ambient air (humidity ~ 50%) for one months without device encapsulation. However, the control devices as well as the devices with EFGnPs-H interlayers were completely degraded after just 10 days at the same conditions, which emphasized the effects of the hydrophobic properties of EFGnPs-F on the device stability.

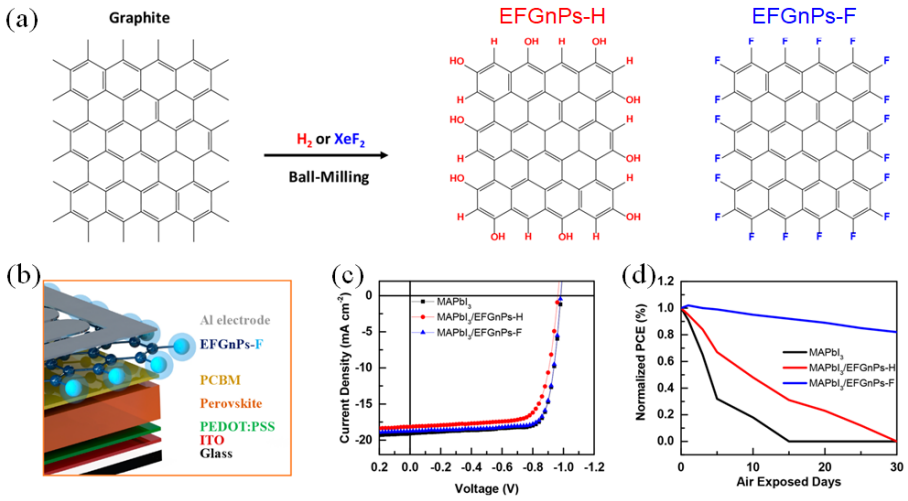

Fig. 17. (a) The hydrogen and fluorine functionalized graphene nanoplatelets (EFGnPs-H and EFGnPs-F) prepared by a mechanochemical ball-milling method. (b) Schematic device diagram showing the PSCs with fluorine functionalized graphene nanoplatelets as electrode interlayers. (c,d) *J-V* characteristics and stabilities of the PSCs with EFGnPs-H and EFGnPs-F layers. Reproduced with permission from ref.[213].

Reduced graphene oxide

Similar with that in normal structure PSCs, the solution processed reduced graphene oxides have been proved to be able to enhance the device performance by doping or simply replacing the traditional organic ETLs (PCBM is mostly often used) in inverted PSCs.[168, 214, 215] Kakavelakis *et al.*[214] first reported the fabrication of highly air stable

planar inverted PSCs with rGO-doped PCBM electron transport layers. It was identified that the addition of rGO in PCBM not only increased its conductivity but also stabilized the perovskite/PCBM interface. As a result, the PSCs with rGO-doped PCBM ETL exhibited a higher PCE of 14.5% with significantly extended stability, compared to 12.9% PCE of the reference cell. Instead of using organic ETLs like PCBM, Nouri *et al*. prepared inverted PSCs with graphene-based inorganic charge transport layers with device configurations of glass/ITO/GO/$MAPbI_3$/GO-Li/TiO_x/Al[168] or glass/ITO/NiO/GO/$MAPbI_3$/GO-Li/TiO_x/Al[215]. Despite the slightly lower efficiencies than the as-prepared PCBM-based devices, these PSCs with inorganic charge transport layers were proved to be much more stable. Further studies about how to improve the efficiencies of PSCs with graphene-based ETLs are needed.

4.2 Transition metal dichalcogenides for electron transporting

Apart from graphene and its derivatives, some other 2D materials, especially transition metal dichalcogenides (TMDs), have also shown obvious advantages for electron transporting in PSCs.[216-218] Wang *et al*.[216] employed ultrathin 2D-interlayers of GO (for hole transporting) and MoS_2 (for electron transporting) simultaneously in the same device for largely enhanced PCE and stability, as shown in Fig. 18. The PSCs consisted a structure of ITO/PEDOT:PSS/GO/perovskite/PCBM/MoS_2/Ag. Insertion of 2D inter-layers was demonstrated to be a feasible way for improving the energy level matching at interfaces of PSCs. In this work, a thin layer of MoS_2 (optimum thickness ~ 3 nm) is thermally evaporated on top of PCBM layer, which reduced the work-function of Ag electrode by about 0.5 eV from Ag (4.7eV) to MoS_2/Ag (4.2 eV) and thereby decreased the energy barrier at the PCBM/Ag interface. Meanwhile, the HOMO of GO film (~ 1-nm thick) matched well with that of PEDOT:PSS and perovskite layers, as shown in Fig. 18b. The better energy-level matching greatly promoted the charge transport and reduced charge recombination at the interfaces. Therefore, when $MAPbI_3$ was used as active layer, the device efficiency was dramatically improved from 14.15% to 19.14% after interfacial modifications with GO and MoS_2, with greatly enhanced V_{oc} (from 0.962 V to 1.135 V), as shown in Fig. 18c. Moreover, the V_{oc} of the device was greatly

increased from 1.010 V to 1.176 V when $MAPbI_{2.5}Br_{0.5}$ was used as active layer, as shown in Fig. 18d. This work indicates that many 2D materials are important candidates for interfacial modifications of PSCs to achieve better energy matching, high device efficiency and good stability. Besides, Yin *et al*.[217] adopted the solution-processed two-dimensional TiS_2 as an effective ETL in planar PSCs with a device structure of FTO/TiS_2/$MAPbI_3$/spiro-OMeTAD/Au, as shown in Fig. 19. A relatively high PCE of 17.37% was obtained with this novel electron transport material, comparable with the efficiency of TiO_2 based reference devices (17.07%). More importantly, compared with the TiO_2-based PSCs, the TiS_2-based ones demonstrated higher photo-stability under continuous UV-light illumination due to the lower photocatalytic properties of TiS_2 films. Almost at the same time, Huang *et al*.[218] also reported the application of TiS_2 as ETL in PSCs with similar device structure. A higher PCE of 18.79% was achieved with mixed perovskites as active materials. These results demonstrate that solution processed TMDs-based ETLs have great promise for fabricating low cost and highly efficient PSCs at low temperature.

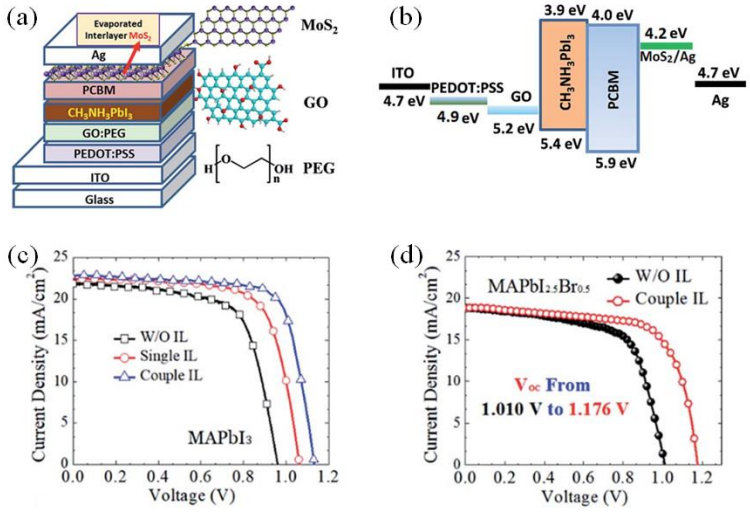

Fig. 18. (a,b) Schematic diagrams of the device structure and the corresponding energy levels. (c) *J-V* curves of $MAPbI_3$-based PSCs with different ILs (inter-layers), in which single IL means with MoS_2 interlayer only, while coupled IL means with both MoS_2 and GO interlayers. (d) *J-V* curves of the $MAPbI_{2.5}Br_{0.5}$-based PSCs. Reproduced with permission from ref.[216].

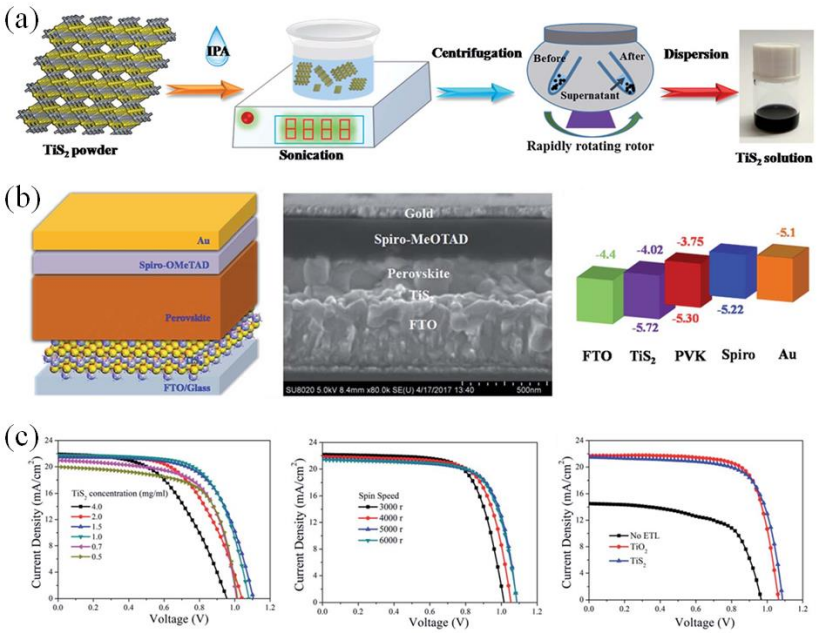

Fig. 19. (a) The liquid-phase exfoliation process of TiS_2 nanosheets. (b) The schematic device structure, cross-sectional SEM image, and energy levels of the PSCs with TiS_2 as ETLs. (c) *J-V* characteristics of the PSCs fabricated at different conditions. Reproduced with permission from ref.[217].

Table 3. Summary of the PSCs with ETLs based on 2D materials.

Normal or Inverted structure	Categories of 2D materials	Planar or Mesoporous	Device structures	PCE (%)	Ref.
Normal	graphene	Mesoporous	glass/FTO/TiO_2+graphene/Al_2O_3/$MAPbI_{3-x}Cl_x$/spiro-OMeTAD/Au	15.6	[188]
Normal	graphene	Planar	glass/FTO/TiO_2+graphene/$Cs_{0.1}MA_{0.9}PbI_3$/spiro-OMeTAD/Au	15.4	[189]
Normal	graphene	Mesoporous	glass/FTO/c-TiO_2/mp-TiO_2+graphene/$MAPbI_3$/spiro-OMeTAD/Au	12.6	[190]
Normal	graphene	Mesoporous	glass/FTO/c-TiO_2/mp-TiO_2+graphene/$MAPbI_3$/GO/spiro-OMeTAD/Au	18.2	[191]
Normal	graphene	Planar	Glass/ITO/SnO_2+graphene/$FA_{0.75}MA_{0.15}Cs_{0.1}PbI_{2.65}Br_{0.35}$/spiro-OMeTAD/Au	20.2	[192]
Normal	graphene	Planar	glass/FTO/c-ZnO/ZnO+graphene/$MAPbI_3$/spiro-OMeTAD/Ag	10.34	[193]
Normal	graphene	Mesoporous	glass/FTO/c-TiO_2/mp-$SrTiO_3$+graphene/$MAPbI_3$/spiro-OMeTAD/Ag	10	[194]
Normal	GQDs	Mesoporous	glass/FTO/c-TiO_2/mp-TiO_2/GQDs/$MAPbI_3$/spiro-OMeTAD/Au	10.15	[196]
Normal	GQDs	Planar	glass/FTO/c-TiO_2/GQDs/$MAPbI_3$/spiro-OMeTAD/Au	19.11	[197]
Normal	GQDs	Mesoporous	glass/FTO/c-TiO_2/mp-TiO_2/GQDs/$CsPbBr_3$/Carbon	9.72	[198]
Normal	GQDs	Planar	glass/ITO/SnO_2+GQDs/$MAPbI_3$/spiro-OMeTAD/Au	20.23	[199]
Normal	GQDs	Planar	glass/ITO/PCBM+GQDs/$MAPbI_3$/spiro-OMeTAD/Au	17.56	[200]
Normal	rGO	Mesoporous	glass/FTO/c-TiO_2/rGO+mp-TiO_2/$MAPbI_3$/spiro-OMeTAD/Ag	14.5	[203]
Normal	rGO	Mesoporous	glass/FTO/rGO+c-TiO_2/rGO+mp-TiO_2/$MAPbI_3$/spiro-OMeTAD/Au	9.3	[204]
Normal	rGO	Mesoporous	glass/FTO/c-TiO_2/rGO+mp-TiO_2/$(FAPbI_3)_{0.85}(MAPbBr_3)_{0.15}$/spiro-OMeTAD/Ag	19.54	[205]
Normal	rGO	Mesoporous	glass/FTO/c-TiO_2/rGO+mp-TiO_2/$MAPbI_{3-x}Cl_x$/GO/CuBuPc/Au	15.9	[153]
Normal	GO-Li	Mesoporous	glass/FTO/c-TiO_2/mp-TiO_2/GO-Li/$MAPbI_3$/spiro-OMeTAD/Au	11.14	[209]

Normal	rGO scaffold	Mesoporous	glass/FTO/c-TiO_2/rGO/$MAPbI_3$/spiro-OMeTAD/Au	17.2	[210]
Normal	rGO	Planar	glass/FTO/rGO+ZnO/$MAPbI_3$/spiro-OMeTAD/Au	15.2	[206]
Normal	rGO	Mesoporous	glass/FTO/c-Zn_2SnO_4/rGO+mp-Zn_2SnO_4/$MAPbI_3$/spiro-OMeTAD/Au	17.89	[207]
Normal	rGO	Mesoporous	glass/ITO/rGO+mp-polyaniline/Cs_2CO_3/$MAPbI_3$/PffBT4T-2OD/Ag	13.8	[208]
Inverted	graphene nanoribbons	Planar	glass/ITO/PEDOT:PSS/$MAPbI_3$/graphene nanoribbons/Al	16.5	[211]
Inverted	3D graphene nanostructures	Planar	glass/ITO/PEDOT:PSS/$MAPbI_3$/3D graphene nanostructures/Ag	18.0	[212]
Inverted	Fluorine Functionalized Graphene	Planar	glass/ITO/PEDOT:PSS/$MAPbI_3$/PCBM/graphene/Al	14.3	[213]
Inverted	rGO	Planar	glass/ITO/PEDOT:PSS/$MAPbI_3$/rGO+PCBM/PFN/Ag	14.5	[214]
Inverted	GO-Li	Planar	glass/ITO/GO/$MAPbI_3$/GO-Li/TiO_x/Al	10.2	[168]
Inverted	GO-Li	Planar	glass/ITO/NiO/GO/$MAPbI_3$/GO-Li/TiO_x/Al	11.2	[215]
Inverted	MoS_2	Planar	glass/ITO/PEDOT:PSS/GO/$MAPbI_3$/PCBM/MoS_2/Ag	19.14	[216]
Normal	TiS_2	Planar	glass/FTO/TiS_2/$MAPbI_3$/spiro-OMeTAD/Au	17.37	[217]
Normal	TiS_2	Planar	glass/ITO/TiS_2/$FA_xMA_{1-x}PbI_{3-y}Br_y$/spiro-OMeTAD/Ag	18.79	[218]

Note: c-TiO_2, c-ZnO and c-Zn_2SnO_4 indicate the compact layers of TiO_2, ZnO and Zn_2SnO_4, while mp-TiO_2 and mp-Zn_2SnO_4 means mesoporous layers of TiO_2 and Zn_2SnO_4. GO and rGO stand for graphene oxide and reduced graphene oxide, respectively. CuBuPc is n-butyl substituted copper phthalocyanine. GO-Li represents Lithium-Neutralized Graphene Oxide.

5. 2D materials in perovskite layer

Crystallization, morphology and grain size of the perovskite films are critical factors that can greatly affect their optoelectronic properties, which may further influence the performances of PSCs. Generally, perovskite films with high crystallinity and large grain size are more desirable to achieve PSCs with higher PCEs and better stability.[39, 48, 219, 220] Therefore, it has been verified that controlling of the nucleation and crystallization process of perovskite films, and passivation of the charge traps at the crystal grain boundaries are effective strategies for achieving high device performances. To do this, one alternative way is introducing 2D materials to the perovskite layer as additives. Table 4 summarizes the recent reported work about the incorporation of 2D materials (including rGO[221], GO[222, 223], GQDs[224] and *g*-C_3N_4[225]) in the perovskite layer, in both normal and inverted PSCs. Hadadian *et al*.[221] first proposed the introduction of nitrogen-doped reduced graphene oxide (N-rGO) in the mixed organic-inorganic halide perovskite layer, by simply dispersing the N-rGO nanosheets in the perovskite precursor solution, as shown in Fig. 20a. The N-rGO incorporated perovskite

films exhibited larger grain size than the control films as observed from the SEM images (Fig. 20b-c), which was originated from the reduced crystallization rate after N-rGO incorporation, as shown in Fig. 20d. Fig. 20e shows part of the liquid-state ^{1}H NMR spectra of the perovskite solution. For the pristine perovskite solution, the peak located at 8.91 ppm was corresponding to the N-H bonding of the FA cations. As observed, this peak showed a downshift after N-rGO addition in the perovskite solution, which was ascribed to the interaction between the H atoms of the FA and basic sites on N-rGO. It was believed that this interaction changed the environment around H atoms of FA cations, and thereby slowed down the crystallization rate, leading to larger grains in the perovskite films. As a result, by the introduction of N-rGO nanosheets in the perovskite layers, all the photovoltaic parameters of the PSCs were improved (see Fig. 20f), and the PCEs were increased from 17.3% to 18.7%. It was confirmed that the increased J_{sc} and FF were attributed to the improved perovskite film with larger grain size and fewer grain boundaries, while the enlarged V_{oc} was due to the passivation of traps by the N-rGO nanosheets at the perovskite/HTL interface. In addition, some reports also presented similar effects of crystallization and morphology controlling as well as grain boundary passivation by using GO flakes, GQDs and 2D polymeric *g*-C_3N_4 as additives in perovskite solution.[222-225] These studies indicate that it is a simple approach to make use of 2D nanostructures as cheap but quite effective additives towards further improvement of the PSCs.

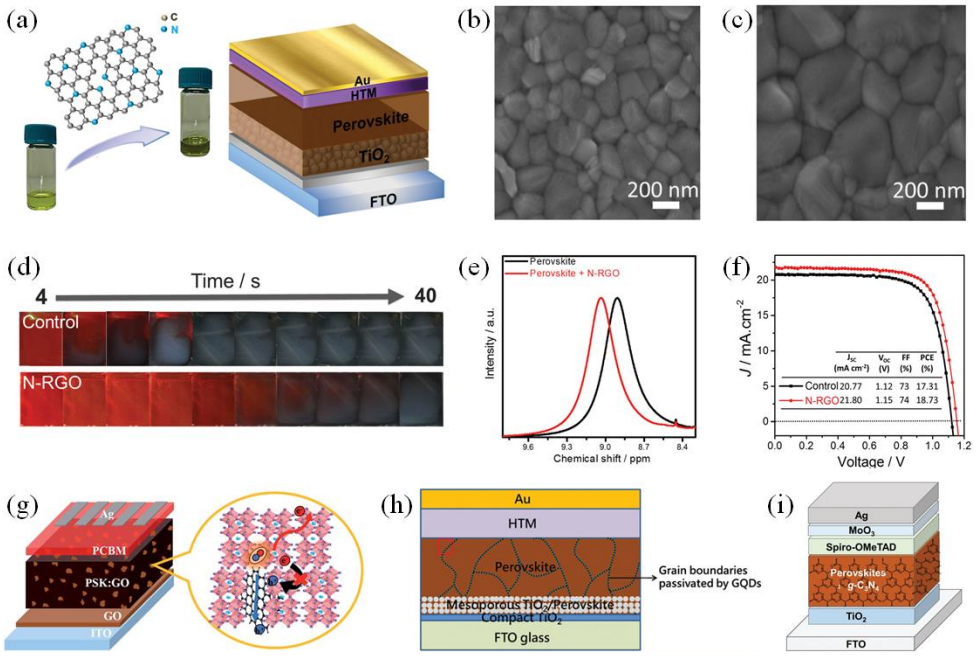

Fig. 20. (a) Schematic diagrams showing the N-RGO doped perovskite solution and the PSC with a structure of FTO/TiO_2/N-rGO+perovskite/spiro-OMeTAD/Au. (b,c) SEM images of perovskite films before and after incorporation of N-rGO. (d) Photographs of perovskite films during the annealing process at 100ºC. (e) 1H NMR spectra of perovskite and N-rGO/perovskite solution. (f) *J-V* characteristics of the control device and N-rGO incorporated device. Reproduced with permission from ref.[221]. (g-i) Schematic diagrams of the PSCs with additives of GO, GQDs and *g*-C_3N_4 in perovskite layers. Reproduced with permission from ref.[222, 224, 225].

Table 4. Summary of the PSCs with 2D materials incorporated in perovskite layer.

Normal or Inverted structure	Categories of 2D materials	Planar or Mesoporous	Device structures	PCE (%)	Ref.
Normal	N-doped rGO	Mesoporous	glass/FTO/c-TiO_2/mp-TiO_2/N-rGO+$(FAPbI_3)_{0.85}(MAPbBr_3)_{0.15}$/spiro-OMeTAD/Au	18.73	[221]
Inverted	GO	Planar	glass/ITO/GO/GO+$MAPbI_3$/PCBM/Ag	15.2	[222]
Normal	GO	Planar	glass/ITO/SnO_2/GO+$MAPbI_3$/spiro-OMeTAD/Au	17.59	[223]
Normal	GQDs	Mesoporous	glass/FTO/c-TiO_2/mp-TiO_2/GQDs+$MAPbI_3$/spiro-OMeTAD/Au	18.34	[224]
Normal	*g*-C_3N_4	Planar	glass/FTO/TiO_2/$MAPbI_3$:*g*-C_3N_4/spiro-OMeTAD/MoO_3/Ag	19.49	[225]

6. Conclusions and perspectives

The organic-inorganic metal halide PSCs have experienced a rapid development in the past decade and have revolutionized the prospects of next-generation photovoltaics. They turned a new leaf in solar cell research due to their high PCEs, easy processing and low material and fabrication costs. The perovskite materials have shown great

potential for a variety of optoelectronic applications not just for photovoltaic devices. Despite of high developing speed, the organic-inorganic hybrid PSC is currently still a fragile new star in the photovoltaic community. There are a variety of challenging issues like low module efficiency, poor reproducibility, poor long-term stability, severe *I-V* hysteresis and toxicity of lead, should be carefully addressed through more research work before commercial applications.

The easy solution process and the wide availability of 2D materials, offer a new strategy for the optimization of PSCs. Recently, applications by combining the outstanding properties of 2D materials and organic-inorganic hybrid perovskite materials have been revealed for the fabrication of high-performance PSCs with impressive operational stability. A variety of 2D materials, like graphene and its derivatives and TMDs, have been successfully used for electrodes, hole or electron transport layers and additives in perovskite layer, for the fabrication of high-performance PSCs, owing to their excellent solution processability, ultrahigh carrier mobilities and tunable work function.

CVD-graphene have been proved to be ideal transparent electrode material because of its high electrical conductivity, high transparency, excellent mechanical flexibility, low-temperature processability, low-cost etc. The CVD graphene electrodes were quite promising as alternatives to the traditional noble metal electrodes (Au, Ag etc.), especially for the applications of efficient semitransparent PSCs and tandem solar cells. The graphene-based electrodes provide a simple but effective solution to the cost reduction and stability enhancement of PSCs, facilitating their commercialization process. Besides, the low-temperature processability and robust mechanical properties of graphene material make it possible to fabricate ultra-flexible PSCs. However, because it often involves transfer process and chemical doping before the utilization of graphene electrodes, the device performances are closely related to the quality and conductivities of the transferred graphene films.

When used as charge transport layers (including HTLs and ETLs), interfacial layers, or

additives in the perovskite layer, 2D materials can efficiently increase carrier mobilities, decrease energy barrier, promote charge transport, retard charge recombination, and improve long-term stability of PSCs. The solution processability of 2D materials offer the possibility of the preparation of uniform 2D films with controlled thickness. The tunable energy levels of 2D materials allows for the precise energy-matching of different layers of the device to enhance charge transport. The hydrophobic nature of these 2D materials as well as the isolating effect from moisture or ionic diffusion, can contribute a lot to the device stability. Introducing 2D materials to the perovskite layer as additives has been verified an effective way to increase the crystallinity and grain size of the perovskite films (by controlling of the nucleation and crystallization process of perovskite films), and alleviate charge trapping at the crystal grain boundaries. Some 2D interlayers may also allow a better crystallinity of the perovskite films grown on top of these 2D materials. However, there are no clear universal fabrication protocols of combing PSCs with 2D materials, and the current efficiencies of the PSCs with incorporation of 2D materials are still inferior to the state-of-art devices.

In summary, the incorporation of 2D materials in PSCs has exhibited promising effects especially the enhanced efficiencies and stabilities. Further improvement in this research field is expected when we can synthesis more suitable 2D materials for modification and optimize the device design by taking advantage of the unique feature of 2D materials. Much attention should be paid to gain deeper insight into the mechanisms of the remarkable impact of 2D materials on the device performance and their interactions with perovskite materials which can lead to synergic effects in the optoelectronic properties of the devices. Moreover, considering that 2D materials are intrinsically flexible, the incorporation of 2D materials in PSCs can lead to high-performance flexible solar cells in the future.

Conflict of interest

The authors declare no conflict of interest.

Acknowledgements

This work is financially supported by the Research Grants Council of Hong Kong, China (project No. B-Q59U) and the Hong Kong Polytechnic University (project No. 1-ZVGH).

Peng You received his PhD degree in 2018 from the Department of Applied Physics at the Hong Kong Polytechnic University under the supervision of Prof. Feng Yan. He is currently working as a research associate in Prof. Feng Yan's group at the Hong Kong Polytechnic University. His research interests are focused on perovskite solar cells, 2D materials and transmission electron microscopy.

Tang Guanqi received his M.S. degree in 2015 from Shandong University. Thereafter, he joined Prof. Feng Yan's research group in the Department of Applied Physics at the Hong Kong Polytechnic University as a PhD candidate. His current research interests focus on device physics and fabrication of high-efficient perovskite solar cell.

Prof. Feng Yan has research interests on thin film transistors, solar cells, 2D materials, organic electronics, biosensors and smart materials. He received his PhD degree in physics from Nanjing University in China. Then he joined the Engineering Department of Cambridge University in Feb 2001 as a Research Associate and joined National Physical Laboratory in UK in April 2006 as a Higher Research Scientist. He became an Assistant Professor at the Department of Applied Physics of the Hong Kong Polytechnic University in September 2006 and was promoted to Full Professor in 2016.

References

1. Kojima, A., et al., *Organometal halid perovskites as visible-light sensitizers for photovoltaic cells.* J. Am. Chem. Soc., 2009. **131**: p. 6050-6051.
2. Best Research-Cell Efficiencies: p. (NREL, 2018); https://www.nrel.gov/pv/assets/images/efficiency-chart-20180716.jpg.
3. Feng, J. and B. Xiao, *Crystal Structures, Optical Properties, and Effective Mass Tensors of $CH_3NH_3PbX_3$ (X = I and Br) Phases Predicted from HSE06.* Journal of Physical Chemistry Letters, 2014. **5**(10): p. 1719-1720.
4. Im, J.H., et al., *6.5% efficient perovskite quantum-dot-sensitized solar cell.* Nanoscale, 2011. **3**(10): p. 4088-4093.
5. Kim, H.-S., et al., *Lead iodide perovskite sensitized all-solid-state submicron thin film mesoscopic solar cell with efficiency exceeding 9%.* Sci. Rep., 2012. **2**: p. 591.
6. Lee, M.M., et al., *Efficient hybrid solar cells based on meso-superstructured organometal halide perovskites.* Science, 2012. **338**: p. 643-647.
7. Heo, J.H., et al., *Efficient inorganic–organic hybrid heterojunction solar cells containing perovskite compound and polymeric hole conductors.* Nat. Photonics, 2013. **7**: p. 486-491.
8. Burschka, J., et al., *Sequential deposition as a route to high-performance perovskite-sensitized solar cells.* Nature, 2013. **499**(7458): p. 316-319.
9. Jeon, N.J., et al., *Solvent engineering for high-performance inorganic-organic hybrid perovskite solar cells.* Nature Materials, 2014. **13**(9): p. 897-903.
10. Jeon, N.J., et al., *Compositional engineering of perovskite materials for high-performance solar cells.* Nature, 2015. **517**(7535): p. 476-480.
11. Zhou, H., et al., *Interface engineering of highly efficient perovskite solar cells.* Science, 2014. **345**(6196): p. 542-546.
12. Yang, W.S., et al., *High-performance photovoltaic perovskite layers fabricated through intramolecular exchange.* Science, 2015. **348**: p. 1234-1237.
13. Saliba, M., et al., *Cesium-containing triple cation perovskite solar cells: improved stability, reproducibility and high efficiency.* Energy Environ. Sci., 2016. **9**: p. 1989-1997.
14. Kim, H.S., S.H. Im, and N.G. Park, *Organolead Halide Perovskite: New Horizons in Solar Cell Research.* Journal of Physical Chemistry C, 2014. **118**(11): p. 5615-5625.
15. Yakunin, S., et al., *Detection of X-ray photons by solution-processed lead halide perovskites.* Nature Photonics, 2015. **9**(7): p. 444-449.
16. Yin, W.J., T.T. Shi, and Y.F. Yan, *Unique Properties of Halide Perovskites as Possible Origins of the*

Superior Solar Cell Performance. Advanced Materials, 2014. **26**(27): p. 4653-4658.

17. De Wolf, S., et al., *Organometallic Halide Perovskites: Sharp Optical Absorption Edge and Its Relation to Photovoltaic Performance.* Journal of Physical Chemistry Letters, 2014. **5**(6): p. 1035-1039.
18. Miyata, A., et al., *Direct measurement of the exciton binding energy and effective masses for charge carriers in organic–inorganic tri-halide perovskites.* Nature Physics, 2015. **11**(7): p. 582-587.
19. Noh, J.H., et al., *Chemical management for colorful, efficient, and stable inorganic-organic hybrid nanostructured solar cells.* Nano. Lett., 2013. **13**(4): p. 1764-1769.
20. Giorgi, G., et al., *Small Photocarrier Effective Masses Featuring Ambipolar Transport in Methylammonium Lead Iodide Perovskite: A Density Functional Analysis.* Journal of Physical Chemistry Letters, 2013. **4**(24): p. 4213-4216.
21. Shi, D., et al., *Low trap-state density and long carrier diffusion in organolead trihalide perovskite single crystals.* Science, 2015. **347**(6221): p. 519-522.
22. Stranks, S.D., et al., *Electron-hole diffusion lengths exceeding 1 micrometer in an organometal trihalide perovskite absorber.* Science, 2013. **342**: p. 341-344.
23. Xing, G.C., et al., *Long-Range Balanced Electron- and Hole-Transport Lengths in Organic-Inorganic $CH_3NH_3PbI_3$.* Science, 2013. **342**(6156): p. 344-347.
24. Dong, Q.F., et al., *Electron-hole diffusion lengths > 175 mu m in solution-grown CH3NH3PbI3 single crystals.* Science, 2015. **347**(6225): p. 967-970.
25. Leijtens, T., et al., *Electronic Properties of Meso-Superstructured and Planar Organometal Halide Perovskite Films: Charge Trapping, Photodoping, and Carrier Mobility.* Acs Nano, 2014. **8**(7): p. 7147-7155.
26. Wehrenfennig, C., et al., *High Charge Carrier Mobilities and Lifetimes in Organolead Trihalide Perovskites.* Advanced Materials, 2014. **26**(10): p. 1584-1589.
27. Valverde-Chavez, D.A., et al., *Intrinsic femtosecond charge generation dynamics in single crystal CH3NH3PbI3.* Energy & Environmental Science, 2015. **8**(12): p. 3700-3707.
28. Eperon, G.E., et al., *Formamidinium lead trihalide: a broadly tunable perovskite for efficient planar heterojunction solar cells.* Energy Environ. Sci., 2014. **7**(3): p. 982-988.
29. Amat, A., et al., *Cation-induced band-gap tuning in organohalide perovskites: interplay of spin-orbit coupling and octahedra tilting.* Nano. Lett., 2014. **14**(6): p. 3608-3616.
30. Geng, W., et al., *First-Principles Study of Lead Iodide Perovskite Tetragonal and Orthorhombic Phases for Photovoltaics.* Journal of Physical Chemistry C, 2014. **118**(34): p. 19565-19571.
31. Jacobsson, T.J., et al., *Exploration of the compositional space for mixed lead halogen perovskites for high efficiency solar cells.* Energy & Environmental Science, 2016. **9**(5): p. 1706-1724.
32. Hao, F., et al., *Anomalous Band Gap Behavior in Mixed Sn and Pb Perovskites Enables Broadening of Absorption Spectrum in Solar Cells.* Journal of the American Chemical Society, 2014. **136**(22): p. 8094-8099.
33. Saliba, M., et al., *A molecularly engineered hole-transporting material for efficient perovskite solar cells.* Nat. Energy, 2016. **1**: p. 1–7.
34. Tang, G.Q., et al., *Performance Enhancement of Perovskite Solar Cells Induced by Lead Acetate as an Additive.* Solar Rrl, 2018. **2**(6).
35. Chao Xie, P.Y., Zhike Liu, Li Li and Feng Yan, *Ultrasensitive Broadband Phototransistors Based on*

Perovskite/Organic-Semiconductor Vertical Heterojunctions. Light: Science & Applications, 2017.

36. Xie, C. and F. Yan, *Enhanced performance of perovskite/organic-semiconductor hybrid heterojunction photodetectors with the electron trapping effects.* Journal of Materials Chemistry C, 2018. **6**(6): p. 1338-1342.
37. Luo, S.Q., et al., *The influence of chloride on interdiffusion method for perovskite solar cells.* Materials Letters, 2016. **169**: p. 236-240.
38. Xiao, Z.G., et al., *Efficient, high yield perovskite photovoltaic devices grown by interdiffusion of solution-processed precursor stacking layers.* Energy & Environmental Science, 2014. **7**(8): p. 2619-2623.
39. Bi, C., et al., *Non-wetting surface-driven high-aspect-ratio crystalline grain growth for efficient hybrid perovskite solar cells.* Nature Communications, 2015. **6**.
40. Wu, C.G., et al., *High efficiency stable inverted perovskite solar cells without current hysteresis.* Energy & Environmental Science, 2015. **8**(9): p. 2725-2733.
41. Dong, Q.F., et al., *Abnormal crystal growth in CH3NH3PbI3-xClx using a multi-cycle solution coating process.* Energy & Environmental Science, 2015. **8**(8): p. 2464-2470.
42. Tai, Q., et al., *Efficient and stable perovskite solar cells prepared in ambient air irrespective of the humidity.* Nat. Commun., 2016. **7**: p. 11105.
43. Tang, K.C., P. You, and F. Yan, *Highly Stable All-Inorganic Perovskite Solar Cells Processed at Low Temperature.* Solar RRL, 2018. **2**(8): p. 1800075.
44. Liu, M., M.B. Johnston, and H.J. Snaith, *Efficient planar heterojunction perovskite solar cells by vapour deposition.* Nature, 2013. **501**(7467): p. 395-398.
45. Choi, J.J., et al., *Structure of Methylammonium Lead Iodide Within Mesoporous Titanium Dioxide: Active Material in High-Performance Perovskite Solar Cells.* Nano Letters, 2014. **14**(1): p. 127-133.
46. Ke, W.J., et al., *Employing Lead Thiocyanate Additive to Reduce the Hysteresis and Boost the Fill Factor of Planar Perovskite Solar Cells.* Advanced Materials, 2016. **28**(26): p. 5214-+.
47. Seo, J.-Y., et al., *Ionic Liquid Control Crystal Growth to Enhance Planar Perovskite Solar Cells Efficiency.* Advanced Energy Materials, 2016: p. 1600767.
48. Nie, W.Y., et al., *High-efficiency solution-processed perovskite solar cells with millimeter-scale grains.* Science, 2015. **347**(6221): p. 522-525.
49. Heo, J.H., et al., *Hysteresis-less inverted $CH_3NH_3PbI_3$ planar perovskite hybrid solar cells with 18.1% power conversion efficiency.* Energy Environ. Sci., 2015. **8**: p. 1602-1608.
50. Wang, Q., et al., *Thin Insulating Tunneling Contacts for Efficient and Water-Resistant Perovskite Solar Cells.* Adv Mater, 2016. **28**(31): p. 6734-9.
51. Novoselov, K.S., et al., *Electric field effect in atomically thin carbon films.* Science, 2004. **306**(5696): p. 666-669.
52. Rao, C.N.R., et al., *Graphene: The New Two-Dimensional Nanomaterial.* Angewandte Chemie-International Edition, 2009. **48**(42): p. 7752-7777.
53. Morozov, S.V., et al., *Giant intrinsic carrier mobilities in graphene and its bilayer.* Physical Review Letters, 2008. **100**(1).
54. Geim, A.K. and K.S. Novoselov, *The rise of graphene.* Nature Materials, 2007. **6**(3): p. 183-191.
55. Lee, C., et al., *Measurement of the elastic properties and intrinsic strength of monolayer graphene.* Science, 2008. **321**(5887): p. 385-388.

56. Nair, R.R., et al., *Fine structure constant defines visual transparency of graphene.* Science, 2008. **320**(5881): p. 1308-1308.
57. Xia, F.N., et al., *Two-dimensional material nanophotonics.* Nature Photonics, 2014. **8**(12): p. 899-907.
58. Balandin, A.A., et al., *Superior thermal conductivity of single-layer graphene.* Nano Letters, 2008. **8**(3): p. 902-907.
59. Bonaccorso, F., et al., *Graphene, related two-dimensional crystals, and hybrid systems for energy conversion and storage.* Science, 2015. **347**(6217).
60. Han, M.Y., et al., *Energy band-gap engineering of graphene nanoribbons.* Physical Review Letters, 2007. **98**(20).
61. Offeman, W.S.H.J.a.R.E., *Preparation of graphitic oxide.* J. Am. Chem. Soc., 1958. **80**: p. 1339.
62. Loh, K.P., et al., *Graphene oxide as a chemically tunable platform for optical applications.* Nature Chemistry, 2010. **2**(12): p. 1015-1024.
63. Eda, G., et al., *Insulator to Semimetal Transition in Graphene Oxide.* Journal of Physical Chemistry C, 2009. **113**(35): p. 15768-15771.
64. Gomez-Navarro, C., et al., *Atomic Structure of Reduced Graphene Oxide.* Nano Letters, 2010. **10**(4): p. 1144-1148.
65. Chhowalla, M., et al., *The chemistry of two-dimensional layered transition metal dichalcogenide nanosheets.* Nature Chemistry, 2013. **5**(4): p. 263-275.
66. Wang, Q.H., et al., *Electronics and optoelectronics of two-dimensional transition metal dichalcogenides.* Nature Nanotechnology, 2012. **7**(11): p. 699-712.
67. Jariwala, D., et al., *Emerging Device Applications for Semiconducting Two-Dimensional Transition Metal Dichalcogenides.* Acs Nano, 2014. **8**(2): p. 1102-1120.
68. Lin, Y. and J.W. Connell, *Advances in 2D boron nitride nanostructures: nanosheets, nanoribbons, nanomeshes, and hybrids with graphene.* Nanoscale, 2012. **4**(22): p. 6908-6939.
69. Watanabe, K., T. Taniguchi, and H. Kanda, *Direct-bandgap properties and evidence for ultraviolet lasing of hexagonal boron nitride single crystal.* Nature Materials, 2004. **3**(6): p. 404-409.
70. Dean, C.R., et al., *Boron nitride substrates for high-quality graphene electronics.* Nature Nanotechnology, 2010. **5**(10): p. 722-726.
71. Liu, H., et al., *Semiconducting black phosphorus: synthesis, transport properties and electronic applications.* Chemical Society Reviews, 2015. **44**(9): p. 2732-2743.
72. Long, G., et al., *Achieving Ultrahigh Carrier Mobility in Two-Dimensional Hole Gas of Black Phosphorus.* Nano Letters, 2016. **16**(12): p. 7768-7773.
73. Tran, V., et al., *Layer-controlled band gap and anisotropic excitons in few-layer black phosphorus.* Physical Review B, 2014. **89**(23).
74. Xia, F.N., H. Wang, and Y.C. Jia, *Rediscovering black phosphorus as an anisotropic layered material for optoelectronics and electronics.* Nature Communications, 2014. **5**.
75. Liu, Z.K., S.P. Lau, and F. Yan, *Functionalized graphene and other two-dimensional materials for photovoltaic devices: device design and processing.* Chemical Society Reviews, 2015. **44**(15): p. 5638-5679.
76. Cai, X., et al., *Preparation of 2D material dispersions and their applications.* Chem Soc Rev, 2018.
77. Li, X.S., et al., *Large-Area Synthesis of High-Quality and Uniform Graphene Films on Copper Foils.* Science, 2009. **324**(5932): p. 1312-1314.

78. Chang, H.X., et al., *Thin Film Field-Effect Phototransistors from Bandgap-Tunable, Solution-Processed, Few-Layer Reduced Graphene Oxide Films.* Advanced Materials, 2010. **22**(43): p. 4872-+.
79. Li, J.H., et al., *Photosensitive Graphene Transistors.* Advanced Materials, 2014. **26**(31): p. 5239-5273.
80. He, R.X., et al., *Solution-Gated Graphene Field Effect Transistors Integrated in Microfluidic Systems and Used for Flow Velocity Detection.* Nano Letters, 2012. **12**(3): p. 1404-1409.
81. Xie, C. and F. Yan, *Perovskite/Poly(3-hexylthiophene)/Graphene Multiheterojunction Phototransistors with Ultrahigh Gain in Broadband Wavelength Region.* Acs Applied Materials & Interfaces, 2017. **9**(2): p. 1569-1576.
82. Sun, Z.H., et al., *Infrared Photodetectors Based on CVD-Grown Graphene and PbS Quantum Dots with Ultrahigh Responsivity.* Advanced Materials, 2012. **24**(43): p. 5878-5883.
83. Xie, C., et al., *Photodetectors Based on Two-Dimensional Layered Materials Beyond Graphene.* Advanced Functional Materials, 2017. **27**(19).
84. Xie, C. and F. Yan, *Flexible Photodetectors Based on Novel Functional Materials.* Small, 2017. **13**(43).
85. Koppens, F.H.L., et al., *Photodetectors based on graphene, other two-dimensional materials and hybrid systems.* Nature Nanotechnology, 2014. **9**(10): p. 780-793.
86. Li, J., et al., *High-Performance, Self-Powered Photodetectors Based on Perovskite and Graphene.* Acs Applied Materials & Interfaces, 2017. **9**(49): p. 42779-42787.
87. Liu, Z.K., et al., *The Application of Highly Doped Single-Layer Graphene as the Top Electrodes of Semitransparent Organic Solar Cells.* Acs Nano, 2012. **6**(1): p. 810-818.
88. Liu, Z.K., J.H. Li, and F. Yan, *Package-Free Flexible Organic Solar Cells with Graphene top Electrodes.* Advanced Materials, 2013. **25**(31): p. 4296-4301.
89. Lin, S.H., et al., *Solution-Processable Ultrathin Black Phosphorus as an Effective Electron Transport Layer in Organic Photovoltaics.* Advanced Functional Materials, 2016. **26**(6): p. 864-871.
90. Liu, Z.K., et al., *Neutral-Color Semitransparent Organic Solar Cells with All-Graphene Electrodes.* Acs Nano, 2015. **9**(12): p. 12026-12034.
91. Liu, S.H., et al., *Black Phosphorus Quantum Dots Used for Boosting Light Harvesting in Organic Photovoltaics.* Angewandte Chemie-International Edition, 2017. **56**(44): p. 13717-13721.
92. Han, T.H., et al., *Extremely efficient flexible organic light-emitting diodes with modified graphene anode.* Nature Photonics, 2012. **6**(2): p. 105-110.
93. Seo, J.W., et al., *Two-Dimensional SnS2 Nanoplates with Extraordinary High Discharge Capacity for Lithium Ion Batteries.* Advanced Materials, 2008. **20**(22): p. 4269-4273.
94. Shi, L. and T.S. Zhao, *Recent advances in inorganic 2D materials and their applications in lithium and sodium batteries.* Journal of Materials Chemistry A, 2017. **5**(8): p. 3735-3758.
95. Luo, B., G. Liu, and L.Z. Wang, *Recent advances in 2D materials for photocatalysis.* Nanoscale, 2016. **8**(13): p. 6904-6920.
96. Akinwande, D., N. Petrone, and J. Hone, *Two-dimensional flexible nanoelectronics.* Nature Communications, 2014. **5**.
97. Zhang, M., et al., *Highly sensitive glucose sensors based on enzyme-modified whole-graphene solution-gated transistors.* Scientific Reports, 2015. **5**.
98. Yan, F., M. Zhang, and J.H. Li, *Solution-Gated Graphene Transistors for Chemical and Biological*

Sensors. Advanced Healthcare Materials, 2014. **3**(3): p. 313-331.

99. Zhang, M., et al., *High-Performance Dopamine Sensors Based on Whole-Graphene Solution-Gated Transistors (vol 7, pg 978, 2014).* Advanced Functional Materials, 2014. **24**(8): p. 1036-1036.
100. Liao, C.Z., et al., *Highly selective and sensitive glucose sensors based on organic electrochemical transistors with graphene-modified gate electrodes.* Journal of Materials Chemistry B, 2013. **1**(31): p. 3820-3829.
101. Sun, Z.P., A. Martinez, and F. Wang, *Optical modulators with 2D layered materials.* Nature Photonics, 2016. **10**(4): p. 227-238.
102. Luo, Q., et al., *All-Carbon-Electrode-Based Endurable Flexible Perovskite Solar Cells.* Advanced Functional Materials, 2018. **28**(11).
103. Domanski, K., et al., *Not all that glitters is gold: metal-migration-induced degradation in perovskite solar cells.* ACS Nano., 2016.
104. Zhao, J.J., et al., *Is Cu a stable electrode material in hybrid perovskite solar cells for a 30-year lifetime?* Energy & Environmental Science, 2016. **9**(12): p. 3650-3656.
105. Meng, X., et al., *Versatility of Carbon Enables All Carbon Based Perovskite Solar Cells to Achieve High Efficiency and High Stability.* Adv Mater, 2018. **30**(21): p. e1706975.
106. Batmunkh, M., et al., *Solution processed graphene structures for perovskite solar cells.* Journal of Materials Chemistry A, 2016. **4**(7): p. 2605-2616.
107. Liu, Z.W., et al., *Rapid preparation of conductive transparent films via solution printing of graphene precursor.* Thin Solid Films, 2018. **657**: p. 24-31.
108. Sung, H., et al., *Transparent Conductive Oxide-Free Graphene-Based Perovskite Solar Cells with over 17% Efficiency.* Advanced Energy Materials, 2016. **6**(3).
109. Liu, Z.K., et al., *Ultrathin and flexible perovskite solar cells with graphene transparent electrodes.* Nano Energy, 2016. **28**: p. 151-157.
110. You, P., et al., *Efficient Semitransparent Perovskite Solar Cells with Graphene Electrodes.* Advanced Materials, 2015. **27**(24): p. 3632-3638.
111. Kim, S., et al., *Effect of layer number on flexible perovskite solar cells employing multiple layers of graphene as transparent conductive electrodes.* Journal of Alloys and Compounds, 2018. **744**: p. 404-411.
112. Yoon, J., et al., *Superflexible, high-efficiency perovskite solar cells utilizing graphene electrodes: towards future foldable power sources.* Energy & Environmental Science, 2017. **10**(1): p. 337-345.
113. Heo, J.H., et al., *Highly flexible, high-performance perovskite solar cells with adhesion promoted AuCl3-doped graphene electrodes.* Journal of Materials Chemistry A, 2017. **5**(40): p. 21146-21152.
114. Heo, J.H., et al., *Super-flexible bis(trifluoromethanesulfonyl)-amide doped graphene transparent conductive electrodes for photo-stable perovskite solar cells.* Journal of Materials Chemistry A, 2018. **6**(18): p. 8251-8258.
115. Mei, A., et al., *A hole-conductor-free, fully printable mesoscopic perovskite solar cell with high stability.* Science, 2014. **345**: p. 295-298.
116. Xu, X., et al., *Hole selective NiO contact for efficient perovskite solar cells with carbon electrode.* Nano. Lett., 2015. **15**(4): p. 2402-2408.
117. Li, Z., et al., *Laminated Carbon Nanotube Networks for Metal Electrode-Free Efficient Perovskite*

Solar Cells. Acs Nano, 2014. **8**(7): p. 6797-6804.

118. Lang, F., et al., *Perovskite Solar Cells with Large-Area CVD-Graphene for Tandem Solar Cells.* Journal of Physical Chemistry Letters, 2015. **6**(14): p. 2745-2750.
119. Zhou, J.X., et al., *Semi-transparent Cl-doped perovskite solar cells with graphene electrodes for tandem application.* Materials Letters, 2018. **220**: p. 82-85.
120. Yan, K.Y., et al., *High-Performance Graphene-Based Hole Conductor-Free Perovskite Solar Cells: Schottky Junction Enhanced Hole Extraction and Electron Blocking.* Small, 2015. **11**(19): p. 2269-2274.
121. Zhu, Y.Y., et al., *Facile synthesis of nitrogen-doped graphene frameworks for enhanced performance of hole transport material-free perovskite solar cells.* Journal of Materials Chemistry C, 2018. **6**(12): p. 3097-3103.
122. Wei, W., et al., *Potassium-chemical synthesis of 3D graphene from CO2 and its excellent performance in HTM-free perovskite solar cells.* Journal of Materials Chemistry A, 2017. **5**(17): p. 7749-7752.
123. Guo, F., et al., *High-performance semitransparent perovskite solar cells with solution-processed silver nanowires as top electrodes.* Nanoscale, 2015. **7**(5): p. 1642-1649.
124. Bailie, C.D., et al., *Semi-transparent perovskite solar cells for tandems with silicon and CIGS.* Energy & Environmental Science, 2015. **8**(3): p. 956-963.
125. Lee, M., et al., *Silver Nanowire Top Electrodes in Flexible Perovskite Solar Cells using Titanium Metal as Substrate.* Chemsuschem, 2016. **9**(1): p. 31-35.
126. Tong, J.H., et al., *Vacuum-free and metal electrode-free organic tandem solar cells.* Applied Physics Letters, 2015. **106**(5).
127. Jiang, F.Y., et al., *Metal electrode-free perovskite solar cells with transfer-laminated conducting polymer electrode.* Optics Express, 2015. **23**(3): p. A83-A91.
128. Bush, K.A., et al., *23.6%-efficient monolithic perovskite/silicon tandem solar cells with improved stability.* Nature Energy, 2017. **2**(4).
129. McMeekin, D.P., et al., *A mixed-cation lead mixed-halide perovskite absorber for tandem solar cells.* Science, 2016. **351**(6269): p. 151-155.
130. Yang, Y., et al., *Multilayer Transparent Top Electrode for Solution Processed Perovskite/Cu(In,Ga)(Se,S)(2) Four Terminal Tandem Solar Cells.* Acs Nano, 2015. **9**(7): p. 7714-7721.
131. Chen, C.C., et al., *Perovskite/polymer monolithic hybrid tandem solar cells utilizing a low-temperature, full solution process.* Materials Horizons, 2015. **2**(2): p. 203-211.
132. Heo, J.H. and S.H. Im, *CH3NH3PbBr3-CH3NH3PbI3 Perovskite-Perovskite Tandem Solar Cells with Exceeding 2.2 V Open Circuit Voltage.* Advanced Materials, 2016. **28**(25): p. 5121-5125.
133. Acik, M. and S.B. Darling, *Graphene in perovskite solar cells: device design, characterization and implementation.* Journal of Materials Chemistry A, 2016. **4**(17): p. 6185-6235.
134. Qi, J., Z. Xingwang, and Y. Jingbi, *SnO2: A Wonderful Electron Transport Layer for Perovskite Solar Cells.* Small. **0**(0): p. 1801154.
135. Liu, J., et al., *A dopant-free hole-transporting material for efficient and stable perovskite solar cells.* Energy Environ. Sci., 2014. **7**: p. 2963-2967.
136. Bi, C., et al., *Non-wetting surface-driven high-aspect-ratio crystalline grain growth for efficient hybrid perovskite solar cells.* Nature Communications, 2015. **6**: p. 7747.
137. Schwierz, F., *Graphene transistors.* Nature Nanotechnology, 2010. **5**: p. 487.
138. Lee, S.-K., et al., *Stretchable Graphene Transistors with Printed Dielectrics and Gate Electrodes.*

Nano Letters, 2011. **11**(11): p. 4642-4646.
139. Huang, M.Q., et al., *Broadband Black-Phosphorus Photodetectors with High Responsivity.* Advanced Materials, 2016. **28**(18): p. 3481-3485.
140. Radisavljevic, B., et al., *Single-layer MoS2 transistors.* Nature Nanotechnology, 2011. **6**: p. 147.
141. Lopez-Sanchez, O., et al., *Ultrasensitive photodetectors based on monolayer MoS2.* Nature Nanotechnology, 2013. **8**: p. 497.
142. Katsnelson, M.I., *Graphene: carbon in two dimensions.* Materials Today, 2007. **10**(1): p. 20-27.
143. Jeon, N.J., et al., *A fluorene-terminated hole-transporting material for highly efficient and stable perovskite solar cells.* Nature Energy, 2018.
144. Cao, J., et al., *Well-Defined Thiolated Nanographene as Hole-Transporting Material for Efficient and Stable Perovskite Solar Cells.* Journal of the American Chemical Society, 2015. **137**(34): p. 10914-10917.
145. Cogal, S., et al., *RF plasma-enhanced graphene–polymer composites as hole transport materials for perovskite solar cells.* Polymer Bulletin, 2018.
146. Ye, J., et al., *Efficient and stable perovskite solar cells based on functional graphene-modified P3HT hole-transporting layer.* Rsc Advances, 2016. **6**(43): p. 36356-36361.
147. Wen, X.R., et al., *Interfacial engineering with amino-functionalized graphene for efficient perovskite solar cells.* Journal of Materials Chemistry A, 2016. **4**(35): p. 13482-13487.
148. Luo, Q., et al., *Iodide-reduced graphene oxide with dopant-free spiro-OMeTAD for ambient stable and highefficiency perovskite solar cells.* J. Mater. Chem. A, 2015. **3**: p. 15996–16004.
149. Yu, J.H., et al., *Synergetic effects of solution-processable fluorinated graphene and PEDOT as a hole-transporting layer for highly efficient and stable normal-structure perovskite solar cells.* Nanoscale, 2017. **9**(44): p. 17167-17173.
150. Li, H., et al., *Enhancing Efficiency of Perovskite Solar Cells via Surface Passivation with Graphene Oxide Interlayer.* Acs Applied Materials & Interfaces, 2017. **9**(44): p. 38967-38976.
151. Selvakumar, D., et al., *Heteroatom doped reduced graphene oxide paper for large area perovskite solar cells.* Solar Energy, 2018. **163**: p. 564-569.
152. Li, W., et al., *Graphene oxide as dual functional interface modifier for improving wettability and retarding recombination in hybrid perovskite solar cells.* Journal of Materials Chemistry A, 2014. **2**(47): p. 20105-20111.
153. Nouri, E., et al., *Improvement of the photovoltaic parameters of perovskite solar cells using a reduced-graphene-oxide-modified titania layer and soluble copper phthalocyanine as a hole transporter.* Physical Chemistry Chemical Physics, 2018. **20**(4): p. 2388-2395.
154. Nouri, E., M.R. Mohammadi, and P. Lianos, *Construction of Perovskite Solar Cells Using Inorganic Hole-Extracting Components.* Acs Omega, 2018. **3**(1): p. 46-54.
155. Hu, X.H., et al., *Air and thermally stable perovskite solar cells with CVD-graphene as the blocking layer.* Nanoscale, 2017. **9**(24): p. 8274-8280.
156. Chen, H., et al., *Extending the environmental lifetime of unpackaged perovskite solar cells through interfacial design*. J. Mater. Chem. A, 2016. **4**: p. 11604-11610.
157. Lee, D.Y., S.I. Na, and S.S. Kim, *Graphene oxide/PEDOT:PSS composite hole transport layer for efficient and stable planar heterojunction perovskite solar cells.* Nanoscale, 2016. **8**(3): p. 1513-1522.
158. Niu, J.Z., et al., *Graphene-oxide doped PEDOT: PSS as a superior hole transport material for high-efficiency perovskite solar cell.* Organic Electronics, 2017. **48**: p. 165-171.

159. Yu, J.C., et al., *Highly efficient and stable inverted perovskite solar cell employing PEDOT:GO composite layer as a hole transport layer.* Scientific Reports, 2018. **8**(1): p. 1070.
160. Giuri, A., et al., *Cooperative Effect of GO and Glucose on PEDOT:PSS for High V-OC and Hysteresis-Free Solution-Processed Perovskite Solar Cells.* Advanced Functional Materials, 2016. **26**(38): p. 6985-6994.
161. Guo, H., et al., *Efficiency enhancement in inverted planar perovskite solar cells by synergetic effect of sulfated graphene oxide (sGO) and PEDOT:PSS as hole transporting layer.* Rsc Advances, 2017. **7**(79): p. 50410-50419.
162. Liu, T.F., et al., *Fine-tuning optical and electronic properties of graphene oxide for highly efficient perovskite solar cells.* Nanoscale, 2015. **7**(24): p. 10708-10718.
163. Wang, S.Y., et al., *Hybrid UV-Ozone-Treated rGO-PEDOT:PSS as an Efficient Hole Transport Material in Inverted Planar Perovskite Solar Cells.* Nanoscale Research Letters, 2017. **12**.
164. Cho, J.S., et al., *Tuning surface chemistry and morphology of graphene oxide by γ-ray irradiation for improved performance of perovskite photovoltaics.* Carbon, 2018. **139**: p. 564-571.
165. Jokar, E., et al., *Anomalous Charge-Extraction Behavior for Graphene-Oxide (GO) and Reduced Graphene-Oxide (rGO) Films as Efficient p-Contact Layers for High-Performance Perovskite Solar Cells.* Advanced Energy Materials, 2018. **8**(3).
166. Yang, Q.D., et al., *Graphene oxide as an efficient hole-transporting material for high-performance perovskite solar cells with enhanced stability.* Journal of Materials Chemistry A, 2017. **5**(20): p. 9852-9858.
167. Bhosale, S.S., et al., *Functionalization of Graphene Oxide Films with Au and MoOx Nanoparticles as Efficient p-Contact Electrodes for Inverted Planar Perovskite Solar Cells.* Advanced Functional Materials, 2018. **28**(37).
168. Nouri, E., M.R. Mohammadi, and P. Lianos, *Inverted perovskite solar cells based on lithium-functionalized graphene oxide as an electron-transporting layer.* Chemical Communications, 2017. **53**(10): p. 1630-1633.
169. Sun, X., et al., *Improved performance of hole-transporting layer-free perovskite solar cells by using graphene oxide sheets as the nucleation centers.* Rsc Advances, 2017. **7**(72): p. 45320-45326.
170. Kim, J., et al., *Stable and null current hysteresis perovskite solar cells based nitrogen doped graphene oxide nanoribbons hole transport layer.* Scientific Reports, 2016. **6**.
171. Li, D., et al., *Graphene oxide modified hole transport layer for CH3NH3PbI3 planar heterojunction solar cells.* Solar Energy, 2016. **131**: p. 176-182.
172. Zhou, Z.M., et al., *Stable Inverted Planar Perovskite Solar Cells with Low-Temperature-Processed Hole-Transport Bilayer.* Advanced Energy Materials, 2017. **7**(22).
173. Luo, H., et al., *Efficient and Air-Stable Planar Perovskite Solar Cells Formed on Graphene-Oxide-Modified PEDOT: PSS Hole Transport Layer.* Nano-Micro Letters, 2017. **9**(4).
174. Feng, S.L., et al., *High-Performance Perovskite Solar Cells Engineered by an Ammonia Modified Graphene Oxide Interfacial Layer.* Acs Applied Materials & Interfaces, 2016. **8**(23): p. 14503-14512.
175. Wang, Y., et al., *Largely enhanced VOC and stability in perovskite solar cells with modified energy match by coupled 2D interlayers.* Journal of Materials Chemistry A, 2018. **6**(11): p. 4860-4867.
176. Yoon, Y., K. Ganapathi, and S. Salahuddin, *How Good Can Monolayer MoS2 Transistors Be?*

Nano Letters, 2011. **11**(9): p. 3768-3773.

177. Splendiani, A., et al., *Emerging Photoluminescence in Monolayer MoS2.* Nano Letters, 2010. **10**(4): p. 1271-1275.
178. Coleman, J.N., et al., *Two-Dimensional Nanosheets Produced by Liquid Exfoliation of Layered Materials.* Science, 2011. **331**(6017): p. 568-571.
179. Capasso, A., et al., *Few-layer MoS_2 flakes as active buffer layer for stable perovskite solar cells.* Adv. Energy Mater., 2016: p. 1600920.
180. Muduli, S.K., et al., *2D black phosphorous nanosheets as a hole transporting material in perovskite solar cells.* Journal of Power Sources, 2017. **371**: p. 156-161.
181. Kim, Y.G., et al., *Atomically thin two-dimensional materials as hole extraction layers in organolead halide perovskite photovoltaic cells.* Journal of Power Sources, 2016. **319**: p. 1-8.
182. George, K., et al., *Extending the Continuous Operating Lifetime of Perovskite Solar Cells with a Molybdenum Disulfide Hole Extraction Interlayer.* Advanced Energy Materials, 2018. **8**(12): p. 1702287.
183. Ruina, D., et al., *Metal–Organic-Compound-Modified MoS2 with Enhanced Solubility for High-Performance Perovskite Solar Cells.* ChemSusChem, 2017. **10**(14): p. 2869-2874.
184. Dasgupta, U., S. Chatterjee, and A.J. Pal, *Thin-film formation of 2D MoS2 and its application as a hole-transport layer in planar perovskite solar cells.* Solar Energy Materials and Solar Cells, 2017. **172**: p. 353-360.
185. Huang, P., et al., *Water-Soluble 2D Transition Metal Dichalcogenides as the Hole-Transport Layer for Highly Efficient and Stable p-i-n Perovskite Solar Cells.* Acs Applied Materials & Interfaces, 2017. **9**(30): p. 25323-25331.
186. Chen, W., et al., *Black Phosphorus Quantum Dots for Hole Extraction of Typical Planar Hybrid Perovskite Solar Cells.* Journal of Physical Chemistry Letters, 2017. **8**(3): p. 591-598.
187. Cao, J., et al., *Well-defined thiolated nanographene as hole-transporting material for efficient and stable perovskite solar cells.* J. Am. Chem. Soc., 2015. **137**(34): p. 10914-10917.
188. Wang, J.T.W., et al., *Low-Temperature Processed Electron Collection Layers of Graphene/TiO2 Nanocomposites in Thin Film Perovskite Solar Cells.* Nano Letters, 2014. **14**(2): p. 724-730.
189. Yang, P., et al., *Cesium-Containing Perovskite Solar Cell Based on Graphene/TiO2 Electron Transport Layer.* Chemistryselect, 2017. **2**(29): p. 9433-9437.
190. Agresti, A., et al., *Graphene Interface Engineering for Perovskite Solar Modules: 12.6% Power Conversion Efficiency over 50 cm(2) Active Area.* Acs Energy Letters, 2017. **2**(1): p. 279-287.
191. Agresti, A., et al., *Graphene-Perovskite Solar Cells Exceed 18% Efficiency: A Stability Study.* Chemsuschem, 2016. **9**(18): p. 2609-2619.
192. Zhao, X.J., et al., *Efficient Planar Perovskite Solar Cells with Improved Fill Factor via Interface Engineering with Graphene.* Nano Letters, 2018. **18**(4): p. 2442-2449.
193. Chandrasekhar, P.S. and V.K. Komarala, *Graphene/ZnO nanocomposite as an electron transport layer for perovskite solar cells; the effect of graphene concentration on photovoltaic performance.* Rsc Advances, 2017. **7**(46): p. 28610-28615.
194. Wang, C., et al., *Graphene/SrTiO3 nanocomposites used as an effective electron-transporting layer for high-performance perovskite solar cells.* Rsc Advances, 2015. **5**(64): p. 52041-52047.
195. Zhang, Z.P., et al., *Graphene quantum dots: an emerging material for energy-related applications and beyond.* Energy & Environmental Science, 2012. **5**(10): p. 8869-8890.
196. Zhu, Z.L., et al., *Efficiency Enhancement of Perovskite Solar Cells through Fast Electron*

Extraction: The Role of Graphene Quantum Dots. Journal of the American Chemical Society, 2014. **136**(10): p. 3760-3763.

197. Ryu, J., et al., *Size effects of a graphene quantum dot modified-blocking TiO2 layer for efficient planar perovskite solar cells.* Journal of Materials Chemistry A, 2017. **5**(32): p. 16834-16842.
198. Duan, J.L., et al., *High-Purity Inorganic Perovskite Films for Solar Cells with 9.72% Efficiency.* Angewandte Chemie-International Edition, 2018. **57**(14): p. 3787-3791.
199. Xie, J.S., et al., *Enhanced Electronic Properties of SnO2 via Electron Transfer from Graphene Quantum Dots for Efficient Perovskite Solar Cells.* Acs Nano, 2017. **11**(9): p. 9176-9182.
200. Yang, Z.R., et al., *Efficient and highly light stable planar perovskite solar cells with graphene quantum dots doped PCBM electron transport layer.* Nano Energy, 2017. **40**: p. 345-351.
201. Zhang, M., et al., *Facile synthesis of water-soluble, highly fluorescent graphene quantum dots as a robust biological label for stem cells.* Journal of Materials Chemistry, 2012. **22**(15): p. 7461-7467.
202. Mueller, M.L., et al., *Slow Hot-Carrier Relaxation in Colloidal Graphene Quantum Dots.* Nano Letters, 2011. **11**(1): p. 56-60.
203. Han, G.S., et al., *Reduced Graphene Oxide/Mesoporous TiO2 Nanocomposite Based Perovskite Solar Cells.* Acs Applied Materials & Interfaces, 2015. **7**(42): p. 23521-23526.
204. Umeyama, T., et al., *Boosting of the Performance of Perovskite Solar Cells through Systematic Introduction of Reduced Graphene Oxide in TiO2 Layers.* Chemistry Letters, 2015. **44**(10): p. 1410-1412.
205. Cho, K.T., et al., *Beneficial Role of Reduced Graphene Oxide for Electron Extraction in Highly Efficient Perovskite Solar Cells.* Chemsuschem, 2016. **9**(21): p. 3040-3044.
206. Tavakoli, M.M., et al., *High Efficiency and Stable Perovskite Solar Cell Using ZnO/rGO QDs as an Electron Transfer Layer.* Advanced Materials Interfaces, 2016. **3**(11).
207. Mali, S.S., et al., *Reduced graphene oxide (rGO) grafted zinc stannate (Zn2SnO4) nanofiber scaffolds for highly efficient mixed-halide perovskite solar cells.* Journal of Materials Chemistry A, 2016. **4**(31): p. 12158-12169.
208. Tong, S.W., et al., *Thermally Stable Mesoporous Perovskite Solar Cells Incorporating Low-Temperature Processed Graphene/Polymer Electron Transporting Layer.* Acs Applied Materials & Interfaces, 2016. **8**(43): p. 29496-29503.
209. Agresti, A., et al., *Efficiency and Stability Enhancement in Perovskite Solar Cells by Inserting Lithium-Neutralized Graphene Oxide as Electron Transporting Layer.* Advanced Functional Materials, 2016. **26**(16): p. 2686-2694.
210. Tavakoli, M.M., et al., *Interface Engineering of Perovskite Solar Cell Using a Reduced-Graphene Scaffold.* Journal of Physical Chemistry C, 2016. **120**(35): p. 19531-19536.
211. Castro, E., et al., *Cove-Edge Nanoribbon Materials for Efficient Inverted Halide Perovskite Solar Cells.* Angewandte Chemie-International Edition, 2017. **56**(46): p. 14648-14652.
212. Peurifoy, S.R., et al., *Three-Dimensional Graphene Nanostructures.* J Am Chem Soc, 2018.
213. Kim, G.H., et al., *Fluorine Functionalized Graphene Nano Platelets for Highly Stable Inverted Perovskite Solar Cells.* Nano Letters, 2017. **17**(10): p. 6385-6390.
214. Kakavelakis, G., et al., *Efficient and Highly Air Stable Planar Inverted Perovskite Solar Cells with Reduced Graphene Oxide Doped PCBM Electron Transporting Layer.* Advanced Energy Materials, 2017. **7**(7).
215. Nouri, E., M.R. Mohammadi, and P. Lianos, *Improving the stability of inverted perovskite solar*

cells under ambient conditions with graphene-based inorganic charge transporting layers. Carbon, 2018. **126**: p. 208-214.

216. Wang, Y.Y., et al., *Largely enhanced V-OC and stability in perovskite solar cells with modified energy match by coupled 2D interlayers.* Journal of Materials Chemistry A, 2018. **6**(11): p. 4860-4867.
217. Yin, G.N., et al., *Low-temperature and facile solution-processed two-dimensional TiS2 as an effective electron transport layer for UV-stable planar perovskite solar cells.* Journal of Materials Chemistry A, 2018. **6**(19): p. 9132-9138.
218. Huang, P., et al., *Room-Temperature and Aqueous Solution-Processed Two-Dimensional TiS2 as an Electron Transport Layer for Highly Efficient and Stable Planar n-i-p Perovskite Solar Cells.* Acs Applied Materials & Interfaces, 2018. **10**(17): p. 14796-14802.
219. Xiao, Z.G., et al., *Solvent Annealing of Perovskite-Induced Crystal Growth for Photovoltaic-Device Efficiency Enhancement.* Advanced Materials, 2014. **26**(37): p. 6503-6509.
220. Bi, C., et al., *Understanding the formation and evolution of interdiffusion grown organolead halide perovskite thin films by thermal annealing.* Journal of Materials Chemistry A, 2014. **2**(43): p. 18508-18514.
221. Hadadian, M., et al., *Enhancing Efficiency of Perovskite Solar Cells via N-doped Graphene: Crystal Modification and Surface Passivation.* Advanced Materials, 2016. **28**(39): p. 8681-8686.
222. Chung, C.C., et al., *Inverted planar solar cells based on perovskite/graphene oxide hybrid composites.* Journal of Materials Chemistry A, 2017. **5**(27): p. 13957-13965.
223. Zhang, X.N., et al., *Graphene oxide as an additive to improve perovskite film crystallization and morphology for high-efficiency solar cells.* Rsc Advances, 2018. **8**(2): p. 987-993.
224. Fang, X., et al., *Graphene quantum dot incorporated perovskite films: passivating grain boundaries and facilitating electron extraction.* Physical Chemistry Chemical Physics, 2017. **19**(8): p. 6057-6063.
225. Jiang, L.L., et al., *Passivated Perovskite Crystallization via g-C3N4 for High-Performance Solar Cells.* Advanced Functional Materials, 2018. **28**(7).